CALPHAD: Computer Coupling of Phase Diagrams and Thermochemistry 88 (2025) 102772

Contents lists available at ScienceDirect

Calphad

journal homepage: www.elsevier.com/locate/calphad

# The power of computational thermochemistry in high-temperature process design and optimization: Part 2 – Pyrometallurgical process modeling using FactFlow

Kyota Poëti[1], Juan-Ricardo Castillo-Sánchez[1], Ugo Mahue, Vincent Rioux-Frenette, Zineb Squalli-Houssaini, Kentaro Oishi, Jean-Philippe Harvey *

*Centre for Research in Computational Thermochemistry (CRCT), Department of Chemical Engineering, Polytechnique Montréal, C.P. 6079, Succursale "Downtown", Montréal, H3C 3A7, Québec, Canada*

ARTICLE INFO

*Keywords:*
Pyrometallurgy
FactSage
ChemApp
Process simulation

ABSTRACT

Computational thermochemistry is an essential tool when it comes to the design of new industrial pyrometallurgical processes. It also enables the optimization of existing processes by analyzing the effect of various operating conditions on key indicators such as the metal recovery, the product composition, the direct emissions and the process overall energy balance. The modeling of these complex processes requires the use of multiple streams and equilibrium reactors in order to perform a large series of thermodynamic calculations. It also needs to account for the kinetic limitations of key chemical reactions. Current thermochemical software restricts users to single equilibrium reactor calculations or necessitates advanced programming knowledge to build customized pyrometallurgical processes.

In this work, we introduce a new process simulation interface called FactFlow, a multi-stream/multi-unit process simulator embedded in the FactSage package. It offers an intuitive and efficient interface for handling streams, performing equilibrium calculations and allowing the use of stream recycling loops. It also uses the extensive thermodynamic databases available in FactSage to describe the energetics of oxides, sulfides, carbides, salts and metallic phases. This new process simulator interface enables the solving of mass and energy balances of a wide range of pyrometallurgical processes related to the primary production of iron and ferroalloys, copper, titanium and more. In this work, this new interface is used to describe four pyrometallurgical processes, i.e. (i) ferrosilicon alloy production using a submerged arc furnace, (ii) the primary production of copper and the impact of E-waste recycling using a Noranda-like process, (iii) the primary titanium production via the Kroll process, and (iv) the production of direct reduction iron ore pellets via the MIDREX process. Results of the simulations performed in this work are systematically compared to data available in the literature.

## 1. Introduction

In the rapidly evolving landscape of industrial extractive metallurgy and recycling operations, many numerical tools are used to design new processes and to optimize existing ones [1–4]. They prove to be a cost-effective approach for analyzing and optimizing pyrometallurgical operations when compared to expensive and time-consuming lab experiments and pilot-scale trials. Numerical approaches which solve overall mass and energy balances are typically deployed via flowsheet interfaces which connect streams to unit operations to model various processes. Such process simulation software include METSIM [5,6], AVEVA [7], Aspen HYSYS [8], SysCAD [9], and the HSC-Sim module in HSC Chemistry [10]. They are commonly used by engineers and scientists to improve plant productivity. These process simulation packages typically require the explicit definition of the extent of reactions as well as the definition of equilibrium constants that need to be respected in unit operations. They also have limited access to thermodynamic models that describe relevant phases and solutions for pyrometallurgical operations (such as slags, mattes, liquid metallic solutions and molten salts). This is a major limitation when it comes to the exploration of new operating conditions, for the accurate description of energy balances and for the quantification of parasitic reactions of pyrometallurgical processes. Currently, SysCAD can be coupled with

* Corresponding author.
*E-mail address:* jean-philippe.harvey@polymtl.ca (J.-P. Harvey).
[1] These authors contributed equally.

https://doi.org/10.1016/j.calphad.2024.102772
Received 27 July 2024; Received in revised form 28 October 2024; Accepted 10 November 2024
Available online 13 December 2024
0364-5916/© 2024 The Authors. Published by Elsevier Ltd. This is an open access article under the CC BY-NC-ND license (http://creativecommons.org/licenses/by-nc-nd/4.0/).

ChemApp to access FactSage databases (as detailed in [11]); however, this requires additional licensing.

Computational thermochemistry (CT) is an essential approach to alleviate these shortcomings. It is based on the constrained Gibbs energy minimization of a system for given imposed equilibrium conditions (typically temperature, pressure and mass balances) [12]. We presented in a prior article the power of CT through a series of illustrative case studies of high-temperature metallurgical unit operations [13]. CT has also been successfully used to determine optimal operating conditions of existing ferrous processes such as blast furnaces [14], electric arc furnaces [15] as well as many non-ferrous applications related to the primary production of nickel, aluminum [16], copper [17], and lead [18]. In fact, CT is the most efficient predictive tool when dealing with pyrometallurgical processes used to extract metals from concentrate at high temperature [19]. FactSage is recognized as a highly reliable CT package [20] and has demonstrated its strength for accurately describing local/global multi-phase equilibria observed in a multitude of pyrometallurgical operations [21]. As a consequence, it is often linked to process simulation flowsheets to improve the accuracy of their mass and energy balances [22–32].

At the moment, the FactSage interface is not designed to model and describe entire processes. Such a task is currently laborious and requires a unit-by-unit approach where streams are individually saved and introduced in sequential equilibrium calculations. The presence of recycling loops and the modification of operating conditions complexify even more the overall simulation procedure. Specific macroprocessing tools have been made available to partially overcome these interface limitations [20]. ChemApp [33,34] is another tool that offers a solution for modeling unit operations while exploiting the FactSage databases. It requires programming skills and lacks graphical intuitiveness for modifying entire process flowsheets. To overcome these challenges, we developed here the FactFlow module, a multi-stream/multi-reactor simulator integrated within the framework of the FactSage software. This thermochemistry simulation tool handles tasks such as solving mass and energy balances, calculating phase equilibria while managing stream recycling loops. It is designed to help engineers in easily deploying CT for the exploration of a wide range of pyrometallurgical processes and operating conditions.

This work (part II) extends the use of CT to the simulation of entire pyrometallurgical processes using this new graphical interface. The examples which are covered in this work are designed to demonstrate various features of this new interface and to highlight the various ways CT can be used to obtain useful information about a given process such as (i) the metal recovery, (ii) the energy consumption, (iii) the partitioning of valuable elements in various liquid phases formed in a reactor, (iv) the identification of optimal conditions to run a process, as well as (v) the quantification of direct emissions from pyrometallurgical operations. The examples which are presented include a two-reactor configuration for the modeling of ferrosilicon alloy production in a submerged arc furnace (Section 3.1), the primary production and recycling of Cu from chalcopyrite and E-waste (Section 3.2), the production of titanium sponges from rutile (Section 3.3) and the modeling of the MIDREX process using hematite pellets and methane as a source of reducing syngas (Section 3.4).

## 2. FactFlow: A thermochemistry process simulator

The FactFlow interface was developed within the Qt Creator Integrated Development Environment (IDE) [35], using the C++ programming language [36]. FactFlow utilizes the ChemApp library to perform equilibrium calculations, using the same backend as the *Equilib* module of FactSage. The Git tool is used for version control, in combination with a remote repository hosted on GitHub. FactFlow provides a user-friendly interface for building process simulation flowsheets using modular nodes (Table 1). These nodes can be easily dragged and dropped onto the flowsheet canvas. Connections between nodes allow for the representation of streams flowing in/out of *Equilibrium reactor* nodes. Equilibrium calculations are performed in these nodes to determine the chemical reactions which occur and the resulting phase assemblages. Mass flows defined in the input streams sequentially move from one node to another. As shown in Table 1, each FactFlow node provides a unique set of functionalities for converting input streams into output streams and simulating the various chemical reactions occurring in a given equilibrium reactor.

Phases which are formed in a given equilibrium reactor can be split (via the *Splitter* node) and individually sent to other equilibrium reactors. Similarly, individual output streams from distinct equilibrium reactors can be mixed together via the *Mixer* node. Among the other features of the interface, the implementation of the recycling loop via the use of a *Recycle* node stands out as a fundamental and essential tool for process modeling. This is particularly remarkable when compared to other CT-based approaches reported in the literature which require users to apply macro-processing to solve continuous recycling loop modeling using thermochemical packages [37–39].

FactFlow also provides functionalities for analyzing a process through the exploration of a range of operating conditions and stream compositions. Any numeric input field such as the temperature of an equilibrium reactor node can be substituted with a range of values/operating conditions. For example, calculations can be performed from an initial temperature "$T_i$" to a final temperature "$T_f$" by steps of $\Delta T = (T_f - T_i)/(\text{number of calculations} - 1)$. This approach can be extended to pressure and mass balance variations, allowing for the calculation of an entire flowsheet as a function of a series of variable process parameters.

## 3. Pyrometallurgical process modeling using CT

This section presents the design of four pyrometallurgical processes through CT. Each pyrometallurgical process is modeled via the construction of a complete flowsheet in the FactFlow interface. These examples are selected to demonstrate how to determine the series of pyrometallurgical unit operations which are required to extract valuable metals from specific feed materials. These feed materials can either be oxide-rich concentrates (such as the concentrate used for the ferrosilicon production in example #1, $TiO_2$ used for the production of titanium in example #3, and hematite-rich pellets used in the MIDREX example #4) or sulfide-rich concentrates (such as chalcopyrite-$CuFeS_2$ in example #2). The operating conditions of each specific unit operation are modulated and their impacts on the overall process are investigated. To do so, phase equilibrium graphs and thermodynamic data are plotted and analyzed. Each example is outlined in a logical, step-by-step approach, allowing for a comprehensive understanding of the operating conditions of real pyrometallurgical processes.

***Hypotheses and assumptions.***

- **Equilibrium is reached** in any given unit operation. When temperature gradients are experienced in a unit (3.1), multiple counter-flow reactors are used.
- **Steady-state is reached**. This implies that there is no accumulation in the process and that the overall mass balances $\sum(m_{in}) = \sum(m_{out})$ are respected at the end of a simulation. This condition is applied when Recycle nodes are used in the simulation.
- **Reaction kinetics are indirectly accounted** for when industrial data are available by applying virtual stream bypasses. This is equivalent to the virtual element concept recently presented by Pelton et al. [40].

**Table 1**
Description of the different nodes available in FactFlow, along with their submenu and related features.

| Node | Submenu | Functionality |
|---|---|---|
| Input 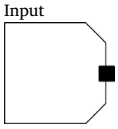 | 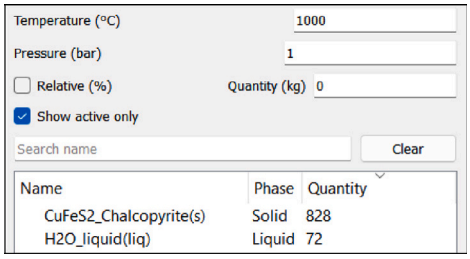  | • Provides an interface to define an input stream by setting the reactant quantities and their input temperature/pressure.<br>• The search toolbar allows users to locate species inside FactSage databases.<br>• The "Show active only" option displays a summary of reactant quantities that are already present in the node.<br>• All input quantities belong to a phase, which ensures that energy balances are maintained. This is equivalent to defining the mass balance with "Initial conditions" enabled in FactSage. |
| Equilibrium Reactor 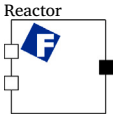 | 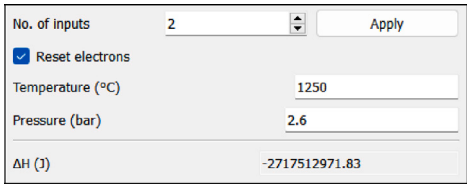  | • Offers the same functionality as the Equilib module in FactSage. *i.e.*, determines the phase equilibrium at user-defined temperature (T) and pressure (P). Additionally, it enables equilibrium calculations with imposed enthalpy change ΔH via the pairs ΔH-T and ΔH-P. This feature is particularly useful for adiabatic calculations, where ΔH=0.<br>• Accepts multiple input streams and produces an output stream. |
| Mixer 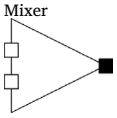 | 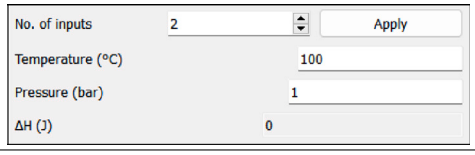  | • Merges streams to produce a single output stream at a user-defined temperature and pressure, without performing an equilibrium calculation.<br>• Calculates a ΔH associated with bringing input streams to the temperature and pressure of the output stream. |
| Splitter 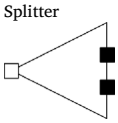 | 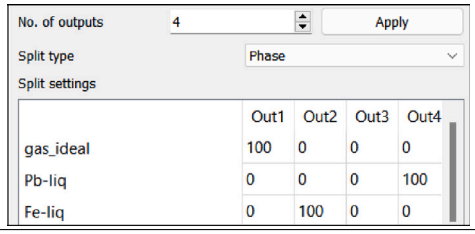  | • Enables the division of a given stream into a user-defined set of output streams based on specified flow percentages.<br>• Splitting modes include: by quantity, by states of matter, and by phases indexed in FactSage. |
| Recycle node 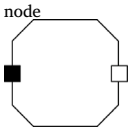 | 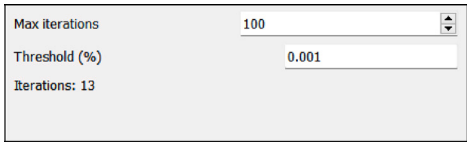  | • Enables mass stream recycling from an output to an earlier stage in the process. This is achieved through a loop convergence method, constrained by a user-defined threshold error.<br>• In case the threshold error is not satisfied, the maximum loop iterations that are permitted are defined by the "Max iteration" setting. |
| Exit 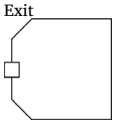 | 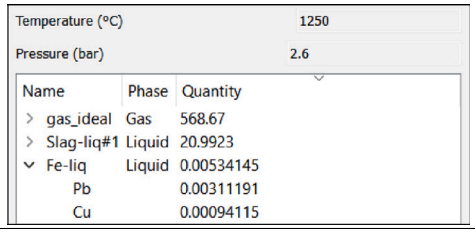  | • Provides an interface for viewing and plotting simulation results. |

### *3.1. Modeling of an electric arc furnace for the production of ferrosilicon using recycling loops*

Ferrosilicons are essential master alloys/reagents used in a wide variety of applications. They can be used for instance:

1. **As an alloying element in steel and cast iron**: Ferrosilicon is employed to increase the silicon concentration of various steels to enhance their strength, wear resistance, elasticity and scale resistance [41]. Silicon is also added to electrical steels (used to produce the core of electromagnetic devices) to reduce their electrical conductivity and magnetostriction. Furthermore, ferrosilicon is added to cast iron to act as inoculants in order to favor graphite precipitation [42].
2. **As a deoxidizing agent in liquid steels**: Some ferrosilicon alloys contain up to 75% silicon by weight (denoted as FeSi75) and are used to deoxidize steel and other iron alloys [41]. In liquid iron, dissolved silicon is oxidized (in the form of $SiO_2$ particles, which float at the surface of the liquid metal and are subsequently fluxed/dissolved into the slag) at a much lower $pO_2$ than iron, allowing for the removal of dissolved monatomic oxygen.
3. **In magnesium primary production**: Ferrosilicon is utilized to reduce calcined dolomite (a reaction called silicothermic reduction) and facilitates magnesium production through the Pidgeon process [43].

The production of ferrosilicon involves the carbo-reduction of quartzite inside a submerged electric arc furnace. This semi-batch process requires the introduction of a mixture of quartzite, carbon-rich reducing agents and iron-bearing materials into the top of the furnace [39]. The molten metal produced from this carbo-reduction is primarily composed of ferrosilicon. It is periodically collected in a ladle for subsequent processing [39,44].

Machulec and Bialik [38,45] reported that the thermodynamic process of ferrosilicon smelting in a submerged arc furnace can be represented by considering two virtual isothermal reactors: a top virtual reactor equilibrated at a lower temperature (***Reactor 1*** in Fig. 1a), and a bottom virtual reactor equilibrated at a higher temperature (***Reactor 2*** in Fig. 1a). This virtual representation of the electric arc furnace allows for approximating the non-isothermal reaction zones which are formed during its operation [38]. The optimizing of this pyrometallurgical process is a complex and challenging task due to the virtual recycling of the gas stream from the bottom reactor to the top reactor as shown in Fig. 1a (stream **R1**). A CO/SiO gas mixture is exhausted by the first reactor (stream **O1**) [38].

The numerical challenge of having to loop the gas stream between these two virtual reactors is easily facilitated with the use of a **Recycle node** in FactFlow (Fig. 1b). As shown in Fig. 1c, these two virtual isothermal reactors (including the virtual recycling of the gas stream **R1**) can be easily connected in the FactFlow interface to simulate this process. In this flowsheet, stream **I1** represents the reactant stream introduced in the reactor at 20 °C, **I2** is a partially reduced stream coming from the top zone of the furnace (containing the condensed phases formed in reactor 1), **O1** is the output gas from the top virtual reactor 1, **O2** represents the slag phase which is discarded, and finally, stream **O3** is the liquid ferrosilicon alloy which is produced by this furnace.

The virtually recycled gas (stream **R1** in Fig. 1) contains CO($g$) and SiO($g$) produced from the following reaction occurring in the bottom virtual reactor:

$$SiO_2(l) + C(s) \rightarrow SiO(g) + CO(g) \quad (1)$$

This gaseous stream promotes the following reactions which lead to the production of a liquid ferrosilicon alloy [46]:

$$SiO(g) + 2C(s) \rightarrow SiC(s) + CO(g) \quad (2)$$

$$2SiO_2(l) + SiC(s) \rightarrow 3SiO(g) + CO(g) \quad (3)$$

$$SiO(g) + SiC(s) \rightarrow 2Si(l) + CO(g) \quad (4)$$

The input composition used to simulate this ferrosilicon electric arc furnace is presented in Fig. 1 (stream **I1**) and was taken from the work of Machulec and Bialik [38,45]. This input stream is based on a reference amount of 1 kmol of $SiO_2$ (in the form of quartzite), along with solid iron, carbon-rich reducing material (which was defined as pure C graphite), calcined dolomite and other minor oxide impurities. The FTOxid database was used to describe oxide-based phases, while the FSstel database (which is a specialized database for the steel industry) was activated to describe the energetics of metallic phases of this system. Additionally, the FactPS database was selected to define the thermodynamic behavior of the gas phase, the pure liquid substances and the pure compounds (including graphite). Reactors 1 and 2 were set to 1665 °C and 1935 °C, respectively. Finally, the **Recycle node** was configured to run 300 loop iterations. The explanation for this is given in the following paragraphs.

Fig. 2 reports the Si recovery (defined here as the ratio between the Si amount in the liquid metallic phase and the Si amount from the main input stream) in the molten metal obtained in reactor 2 (representing the FeSi75 alloy obtained from a typical submerged arc furnace [38]) as a function of the recycling loop iteration. It indicates that a relatively constant Si recovery is obtained after 50 loop cycles. These findings are consistent with the studies by Machulec and Bialik [45]. These authors used the HSC software and Excel to solve the Gibbs energy minimization problem needed to evaluate all the phase equilibria in their flowsheet. Their simulations resulted in a converged Si recovery of 0.88 after 50 iterations [45].

**Table 2**
Composition of the ferrosilicon alloy at 1935 °C (stream O3 in Fig. 1 before cooling at 1665 °C) obtained through a two-stage reactor configuration after 300 loop iterations. Results are compared to the values reported by Machulec and Bialik at 1935 °C [38,45] with 50 loop iterations.

| Element | Composition (wt%) | |
|---|---|---|
| | This work (300 iterations) | Machulec and Bialik [38,45] (50 iterations) |
| Si | 73.99 | 75.00 |
| Fe | 23.89 | 23.80 |
| Al | 1.73 | 1.04 |
| Ca | 0.28 | 0.14 |
| C | 0.06 | – |
| Mg | 0.03 | 0.02 |
| Ti | 0.01 | 0.01 |
| O | 0.01 | – |

The symbol "–" indicates that the value was not disclosed in [38,45].

The asymptotic Si recovery reached after 50 iterations in the simulation performed by Machulec and Bialik [45] appears valid when compared to the Si recovery curve presented in Fig. 2. A deeper analysis of the phase assemblage as a function of the recycling loop iteration shows however that the steady-state is not reached after 50 iterations (see Fig. 3). According to this figure, the amount of gas exiting reactor 2, the SiC transferred from reactor 1 to reactor 2, and the slag amount produced in reactor 1 (a miscibility is predicted to occur under these equilibrium conditions in this zone) are not reaching their steady state values after 50 cycles. Our simulations show that converged values are reached after 250 iterations. In FactFlow, a threshold convergence error is implemented in a holistic way, *i.e.*, for a given threshold "$e_{target}$", the algorithm scans the mass of each output component ($m_i$) at iteration $i$ and compares it with the results from the previous loop iteration ($m_{i-1}$) using the formula $e_i = |(m_i - m_{i-1})|/m_i \times 100$. The loop continues iterating until the condition $e_i \leq e_{target}$ is met for all output components, ensuring that the convergence criterion is respected.

Table 2 summarizes the simulation results for the ferrosilicon alloy formed after 300 iterations using FactFlow. The ferrosilicon alloy is primarily constituted of Si, Fe, and Al, with the presence of minor impurities (such as Ca, C, Mg, Ti and O). These findings are consistent with the simulation data reported by Machulec and Bialik [38,45]. The minor differences are mainly due to the difference in the accuracy of the thermodynamic databases used by HSC and FactSage respectively. As a striking observation, the thermodynamic model of the metallic ferrosilicon liquid solution accounts for the solubility of both C and O in FactSage. In the work of Machulec and Bialik [38,45] the concentration of these two impurities is not reported.

FactFlow also enables the easy computation of the enthalpy change of the entire system. In the context of the ferrosilicon production, the evaluation of the variation of this state property enables the quantification of energy consumption in the submerged arc furnace. Fig. 4 shows the energy requirement as a function of the recycling loop iteration. This figure indicates that the energy demands do not significantly change at 50 and 300 iterations, which is compatible with the Si recovery in the molten metal being almost the same at 50 and 300 iterations (Fig. 2). Machulec and Bialik [45] used Excel Visual Basic macros to compute the energy consumption after 50 iterations, using the identical feedstock as this study. They reported a theoretical value of 7036.61 kWh/tonne of alloy or 7996.15 kWh/tonne of alloy when considering a thermal efficiency of the furnace $\eta$ of 0.88. This work converges to a theoretical energy consumption of 6190 kWh/tonne of alloy without considering the furnace efficiency ($\eta = 1$), which is in the same order of magnitude as the values reported by Machulec

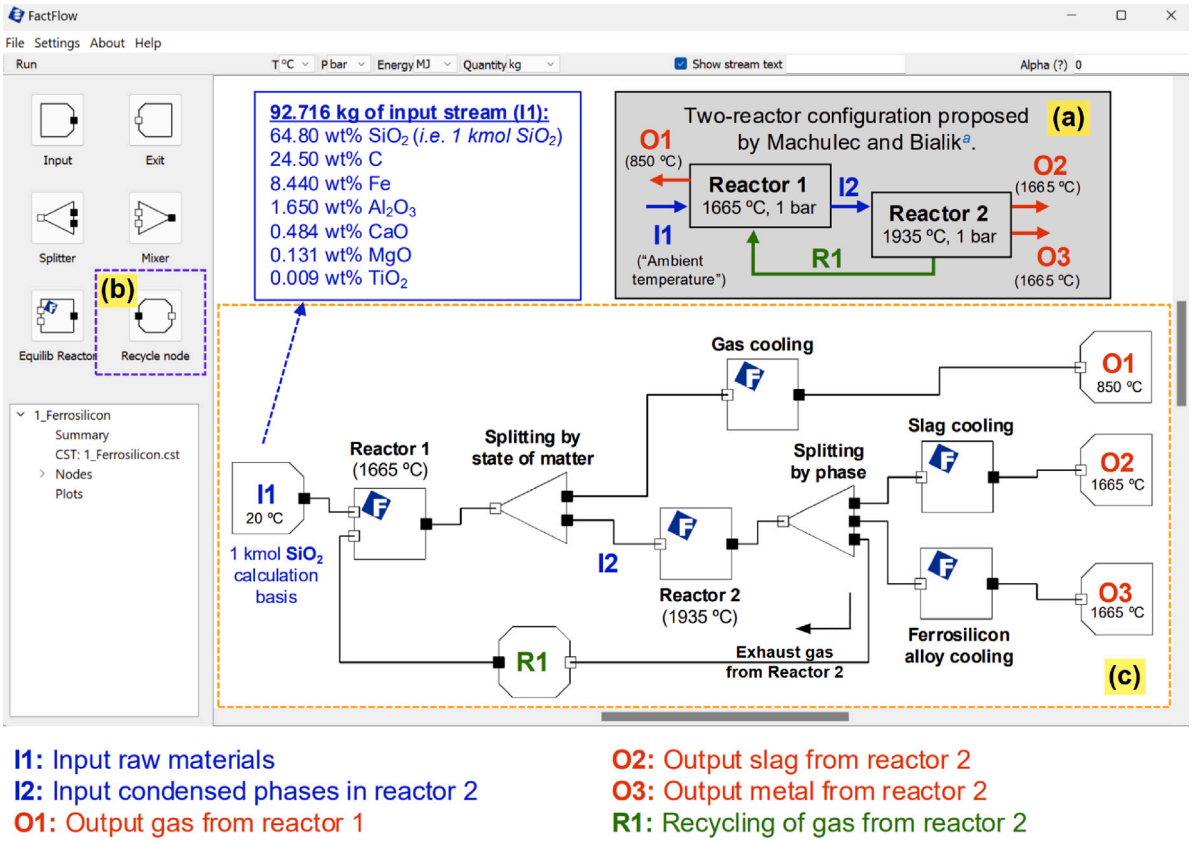


**Fig. 1.** FactFlow interface for Fe-Si alloy production. (a) The inset figure shows the schematics of the two virtual reactors approach for ferrosilicon smelting proposed by Machulec and Bialik ([a][45]). (b) Purple square highlighting the **Reclycle node** icon in FactFlow interface. (c) Two-reactor configuration for ferrosilicon smelting modeling in FactFlow.

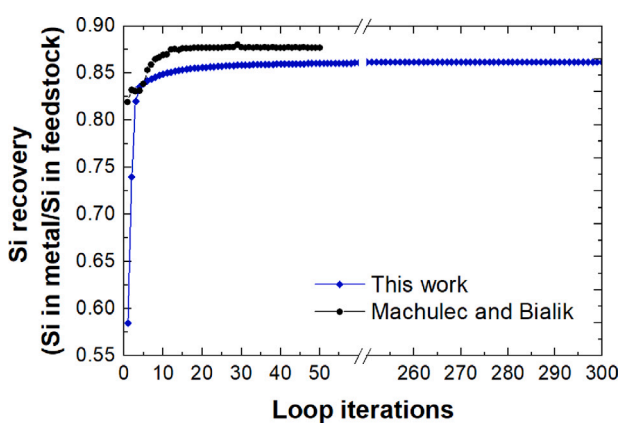


**Fig. 2.** Si recovery in molten metal via FactFlow (blue line), compared to data from Machulec and Bialik using the HSC software and Excel [45] (black line).

and Bialik [45]. We also evaluated the energy requirement if the residual energy of the individual hot output streams upon cooling is not utilized (for preheating input streams for example). A substantially higher energy requirement of 7655 kWh/tonne was obtained in this scenario (open blue circles in Fig. 4). Unlike the approach proposed by Machulec and Bialik [45], where enthalpy changes were calculated individually for each reactor and for each stream cooling, FactFlow directly computes the global enthalpy change between the output and input streams, simplifying computation and enhancing accuracy by reducing potential cumulative errors.

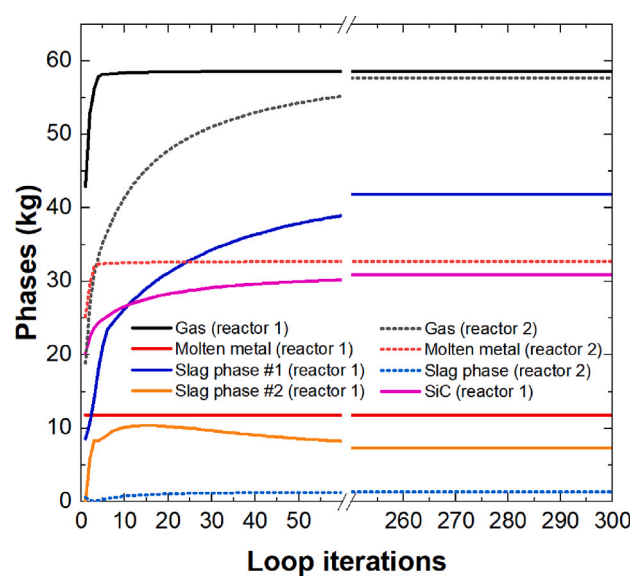


**Fig. 3.** Evolution of phase amounts (kg) in reactor 1 (solid lines) and reactor 2 (dashed lines) as a function of the number of loop iterations.

### 3.2. Cu primary metal production from chalcopyrite and E-waste

Copper is an essential metal for many industries due to its outstanding electrical and thermal conductivity, malleability, and corrosion resistance [47–49]. In nature, it is primarily found in the form of

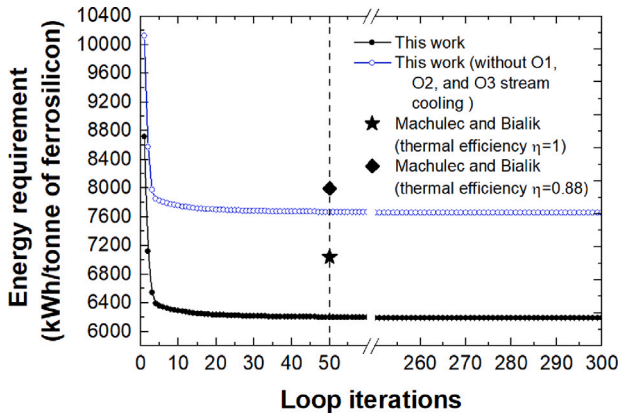


**Fig. 4.** Energy requirement (endothermic) derived from the enthalpy change directly calculated by FactFlow (filled black circles), compared to predictions from Machulec and Bialik [45] with thermal efficiencies ($\eta$) of 0.88 (diamond symbol) and 1 (star symbol). The blue open circles represent the enthalpy change if the cooling of the streams O1, O2 and O3 in Fig. 1 is not considered.

sulfides (*e.g.*, chalcopyrite), oxides, carbonates, sulfates and hydrosilicates [47]. Sulfide ores are typically extracted through pyrometallurgy, while oxide minerals commonly undergo hydrometallurgical operations [47]. Electronic waste recycling, which can represent between 10%–15% of the mass introduced into primary Cu smelters, is another important source of copper. This integration of end-of-life products into primary smelters has been achieved through advanced metallurgical operations, such as the Horne smelter in Quebec, Canada, coupled to the Noranda converter and capable of processing copper sulfide ores along with electronic scrap in the feedstock [50–52].

The flowchart for copper production in a Noranda-like process is presented in Fig. 5 (top). It consists of three main reaction stages (*i.e.*, smelting, slag-forming and copper-making), where the reactors are supplied with wet chalcopyrite-$CuFeS_2$ (containing 8% $H_2O$ [47]), $O_2$-enriched air and $SiO_2$ as a fluxing agent. The bottom of Fig. 5 illustrates the Noranada process which has been modeled using FactFlow. The composition and feed amount for each input stream used in our simulations are reported in Table 3. This work illustrates the smelting (Section 3.2.1) and converting (Section 3.2.2) processes. Additionally, it explores the recycling of electronic waste (E-waste) from portable audio scrap in Section 3.2.3.

### 3.2.1. Smelting

The purpose of the smelting step is to generate a multi-phase assemblage enabling the removal of Fe from the sulfide-based feedstock. This is achieved through the oxidation of iron and sulfur in the chalcopyrite-$CuFeS_2$-rich concentrate within a smelter, typically operating at 1250 °C [47]. As simplified in stoichiometric reaction (5), two condensed phases are generated through this operation, *i.e.*, a matte phase (sulfide-base) and a slag phase (oxygen-based phase). Slag is lighter than matte, thus the matte phase is found at the bottom of the smelter [53]. The outlet gas linked to this operation contains $SO_2$ (reaction (5)) and it is commonly captured to produce sulfuric acid [47].

$$2CuFeS_2(s) + 3.25O_2(g) \rightarrow Cu_2S\text{–}0.5FeS(l) + 1.5FeO(s) + 2.5SO_2(g) \quad (5)$$

Apart from oxygen, silica is employed as a fluxing agent promoting the formation of the slag phase via reaction (6):

$$2FeO(s) + SiO_2(s) \rightarrow Fe_2SiO_4(l) \quad (6)$$

The thermodynamic description of each phase associated with reactions (5) and (6) are stored within the specialized databases of FactSage. In this example, the FTmisc, FToxid and FactPS databases are activated. The matte phase model (sulfide-base) is useful to describe the feedstock and it is stored within the FTmisc database. FToxid includes models of solid and molten oxide-based solutions, thus it contains the slag phase, which is an important output as shown in Fig. 5a. Finally, FactPS contains information on stoichiometric compounds, pure solid/liquid substances and the model for the gas phase.

By considering a 1 tonne basis of $CuFeS_2$ with 8% $H_2O$, reacting with a variable amount of 40 vol.%-$O_2$ air as reported by Davenport et al. [47], the obtained phase assemblage at 1250 °C is presented in Fig. 6. It is shown that the feedstock evolves to a matte/gas equilibrium if $O_2$-enriched air is not incorporated (x-axis = 0) in the reactor. In this initial state, the gas phase mainly corresponds to the evaporated water initially contained in the humid chalcopyrite. By incorporating $O_2$-enriched air in the smelter, the slag phase appears at $x$-axis ~ 140 kg per 1000 kg of feedstock and mainly contains Fe in the form of FeO, FeS, $Fe_2O_3$ and $Fe_2S_3$. For $x$-axis > 500 kg per 1000 kg of feedstock, the spinel phase is the primary oxide-rich phase formed by the interaction of Fe in the matte phase with oxygen.

As reported by Davenport et al. [47], the smelting method employed at the Noranda Smelter (Canada) enables the concentration of copper up to 70 wt% in the matte phase. Fig. 7 illustrates the elemental composition of the matte phase as a function of reacted air (x-axis), indicating that around 700 kg of air per 1000 kg of feedstock is required to achieve the desired 70 wt% Cu.

Besides oxygen, silica plays an important role as a fluxing agent to promote slag formation (reaction (6)), essential for effective Fe transfer in molten phases. In a specific scenario involving 680 kg of $O_2$-enriched air and 1000 kg of wet chalcopyrite (with 8wt% $H_2O$), the undesirable spinel phase appeared in the phase assemblage (Fig. 6). As shown in Fig. 8, the spinel phase (purple line) can be converted to a slag phase (orange line) by adding $SiO_2$ into the smelter. Specifically, an amount of 100 kg of $SiO_2$/1000 kg of humid chalcopyrite ensures that the spinel phase no longer appears in the equilibrium phase assemblage. Considering these conditions, the resulting matte contains around 72 wt% of Cu. Schlesinger et al. [54] reported that 122 kg of $SiO_2$ per 1000 kg of Cu-concentrate (28 wt% Cu) are employed in the Noranda Smelter (Canada). The quantity of $SiO_2$ found in this work is in agreement with the value of these authors considering the simplified chemistry of the feed material which was used, and the absence of basic oxide fluxes typically added to ease the melting process of the oxides present in the smelter [55]. Finally, the gas phase consists primarily of $SO_2$ (reaction (5)) and evaporated water from the initial humid chalcopyrite. Table 3 provides a summary of the final simulation inputs and outputs for smelting.

Table 3 also reports the enthalpy change for the imposed mass balance and operational conditions in the smelting process, indicating a theoretical exothermic operation of the smelting furnace with $\Delta H = -271$ MJ. It is worth noting that without the moisture in the chalcopyrite, the furnace would exhibit a more exothermic behavior ($\Delta H = -692$ MJ). This means that nearly 61% of the energy released by the reaction is used to evaporate the 80 kg of water contained in the 1 tonne of humid chalcopyrite. This highlights the advantage of utilizing the energy generated by the reaction to evaporate water from the concentrate before proceeding to the converting step.

### 3.2.2. Converting

The resulting matte from the smelting stage must undergo subsequent treatment in the so-called converters for *slag-forming* (Converter 1 in Fig. 5) and *copper-making* (Converter 2 in Fig. 5). The *slag-forming* reaction promotes the removal of Fe from the matte phase, via the following reactions [47]:

$$\underline{FeS}_{matte} + 1.5O_2(g) \rightarrow \underline{FeO}_{slag} + SO_2(g) \quad (7)$$

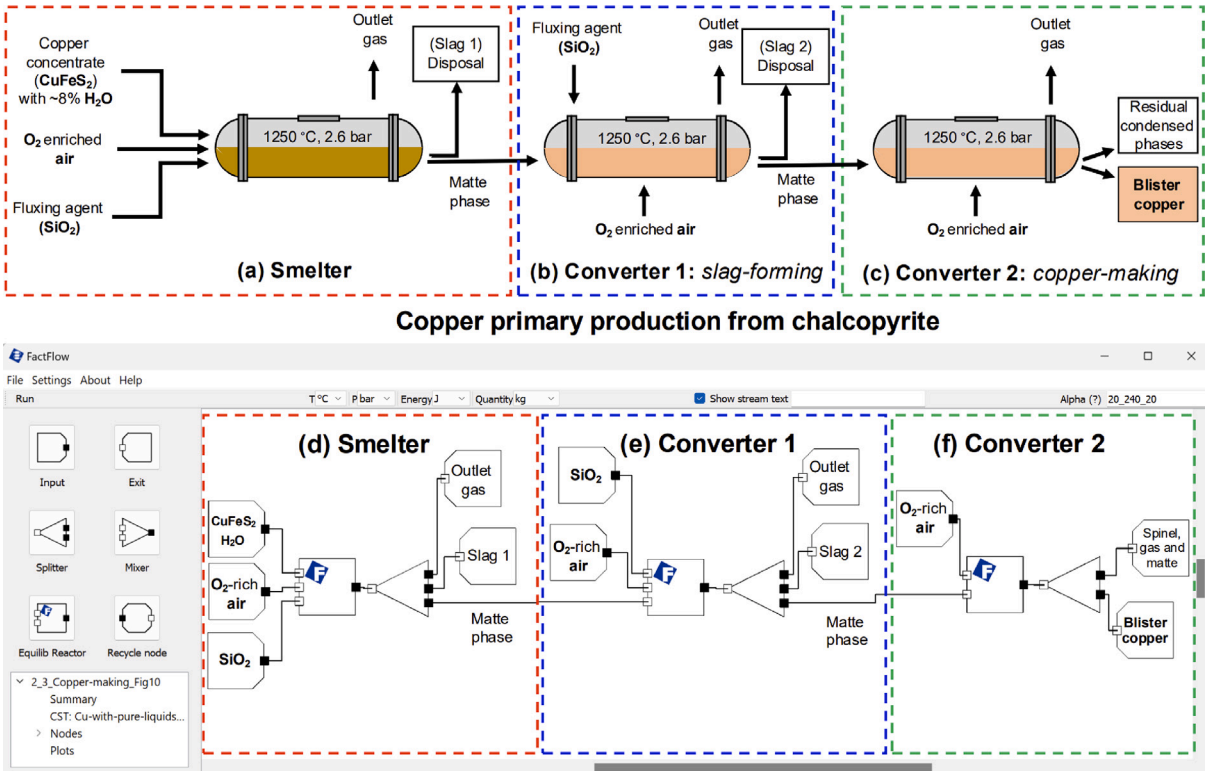


**Fig. 5.** Flowchart for the primary production of copper from chalcopyrite (top), and the equivalent process chart in FactFlow (bottom).

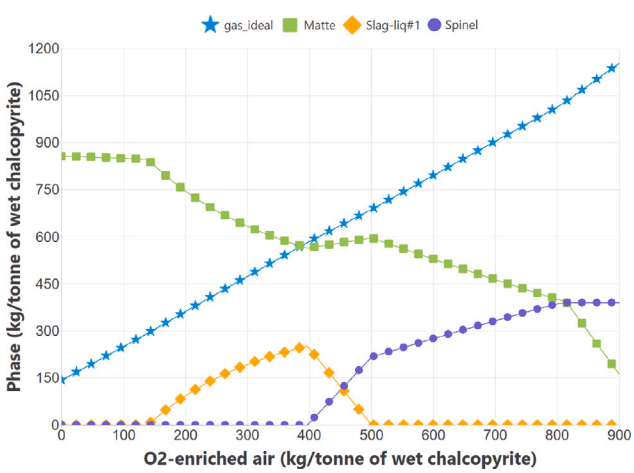


**Fig. 6.** (a) Phase assemblage plot in the smelter considering 1 tonne of wet chalcopyrite and a variable amount of $O_2$-enriched air (x-axis) added to the smelter.

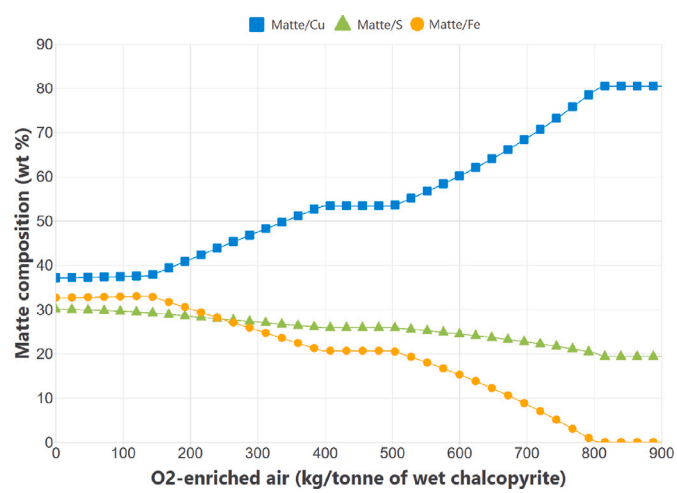


**Fig. 7.** (a) Elemental composition of the matte phase as a function of the injected air in the smelter (x-axis).

$$3\underline{FeS}_{matte} + 5O_2(g) \rightarrow Fe_3O_4(s) + 3SO_2(g) \quad (8)$$

In this study, 435.19 kg of smelting matte with a copper concentration of 72 wt% (as detailed in Table 3) were considered for the *slag-forming* step which was reacted with another stream of $O_2$-enriched air. Fig. 9a illustrates how the composition of the matte evolves as a consequence of the oxidation of iron and its subsequent transfer to an oxide-rich phase. The graphical representation clearly indicates that introducing 60 kg of $O_2$-enriched air yields the suitable matte composition, resulting in a minimal Fe concentration below 1 wt%. This is consistent with existing literature, where the *slag-forming* step is commonly reported to reduce Fe content in the matte phase to approximately ~1 wt% [47]. Additionally, $SiO_2$ should be supplied to the converter to promote the production of the slag phase over the magnetite-spinel phase. Fig. 9b shows the evolution of the phase assemblage with fluxing agent additions (x-axis). This plot shows that adding 17 kg of Si transforms the magnetite-spinel phase into the slag phase, with a small excess of $SiO_2$ in the form of tridymidite forming (refer to Table 3). According to the equilibrium calculation, a total of 389.80 kg of matte/tonne of feedstock with a 79.84 wt% of Cu is produced (Table 3). As shown in Fig. 5f, the matte phase is subsequently subjected to the *copper-making* stage. This is modeled in FactFlow using a *splitter* node. The *copper-making* reactions are [47]:

$$\underline{Cu_2S}_{matte} + 1.5O_2(g) \rightarrow Cu_2O(l) + SO_2(g) \quad (9)$$

$$\underline{Cu_2S}_{matte} + 2Cu_2O(l) \rightarrow 6Cu(l) + SO_2(g) \quad (10)$$

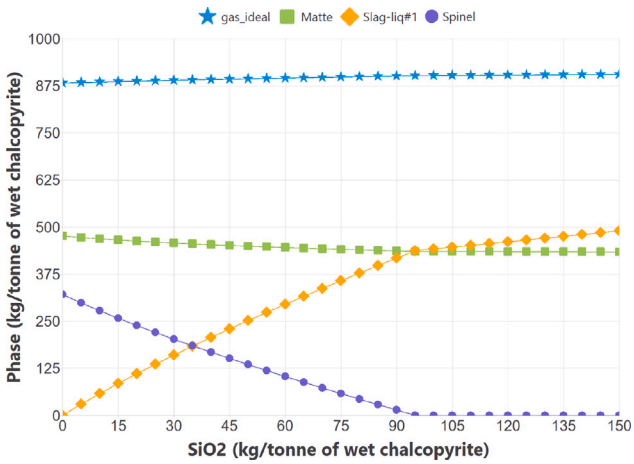


**Fig. 8.** (a) Phase assemblage evolution upon $SiO_2$ additions (x-axis) for a smelter processing **1000 kg** of chalcopyrite (with 8 wt% of $H_2O$) and considering 680 kg of air reacting with the matte phase.

$$\underline{Cu_2S}_{matte} + O_2(g) \rightarrow 2Cu(l) + SO_2(g) \tag{11}$$

Fig. 10a shows the phase assemblage evolution during the *copper-making* step, demonstrating the impact of $O_2$-enriched air injection in the converter (Fig. 5f). As air injection increases, the matte phase (green line) transforms into the molten copper phase (red line). For air inputs greater than 180 kg, the undesired slag phase appears, which must be avoided because of its negative impact on the copper recovery.

In parallel, Fig. 10b details the composition of the Cu-rich liquid in relation to the quantity of air injected within the converter. Remarkably, the optimal condition for achieving a 99.6 wt% Cu purity is precisely at 180 kg of $O_2$-enriched air per 389.80 kg of matte from the *slag-forming*. However, it is noteworthy that beyond this threshold, the oxygen content begins to rise, presenting an undesired outcome. Consequently, industrial operations strategically stop the process just before this occurrence. This investigation suggests that using 170 kg of air minimizes oxygen content and produces an acceptable sulfur content of 1.69 wt%, while also yielding a copper concentration of up to 98 wt% Cu (refer to Table 3). This graphical approach approximation highlights the delicate balance required to optimize copper purity while mitigating undesirable oxygen and sulfur content.

### 3.2.3. Fate of metals using 10 wt% recycling of E-waste

The increase in E-waste generation represents a valuable metallic source, with up to 17.4% being recycled globally in 2019 [56]. Approximately 30% of copper production comes from recycled sources [57]. Thus, thermodynamic modeling of copper recycling is vital for understanding metal partitioning between the various phases during copper-making operations, promoting efficient and sustainable practices. This section exemplifies portable audio scrap recycling, specifically accounting for 10% (mass) of E-waste (Table 4), along with 90% of wet chalcopyrite in the feedstock treated via the Noranda process (Fig. 5).

The composition of E-waste from portable audio scrap used in this study (Table 4) was obtained from Tabelin et al. [58]. This composition includes copper, aluminum, lead, iron, nickel, and silver; however, the content of non-metallic materials was not specified. Consequently, the remaining mass balance was allocated to carbon (graphite) to represent the plastics and other non-metallic materials present in the E-waste scrap. The current thermodynamic model for the matte phase in FactSage does not include silver in its list of optimized solution components. To address this limitation, the pure $Ag_2S(l)$ from the FactPS database has been added as an ideal *end-member* of the matte phase using the *merge* option in FactSage. Similarly, $Ag(l)$ has been appended as an ideal *end-member* of the Cu-rich liquid solution to account for the presence of silver in the final blister copper.

Fig. 11 presents thermodynamic simulation results for blister copper production using 1-tonne feedstock of 10/90 (wt%/wt%) E-waste/wet chalcopyrite. The phase assemblage is sketched across successive stages: smelting, slag-forming (processing the matte phase from smelting) and copper-making (processing the matte phase from slag-forming). Additionally, the fate of metals in these phases, relative to their initial quantities in the feedstock, is presented. Due to the inclusion of E-waste, the temperature for converting (slag-forming and copper making) was elevated to 1300 °C, as opposed to the 1250 °C used when the feedstock consisted solely of chalcopyrite (Section 3.2.2). This adjustment was made to ensure the formation of the slag phase during the slag-forming step. Otherwise, the spinel phase would become the stable phase for the oxide species due to the presence of impurities. Literature on copper smelting, particularly concerning impurities, consistently reports data at 1300 °C [57], indicating widespread adoption of this temperature in similar operations.

Faraji et al. [59] reported a simplified flowchart of Xstrata Copper's Horne smelter in Quebec (also known as the Noranda smelter) for waste printed circuit boards (WPCBs) recycling. The flowchart suggests that Fe, Al, and Pb from the E-waste are transferred to the slag phase, with some Pb exiting the reactors in the form of fumes. These findings align with our thermodynamic simulations, where Al is specifically

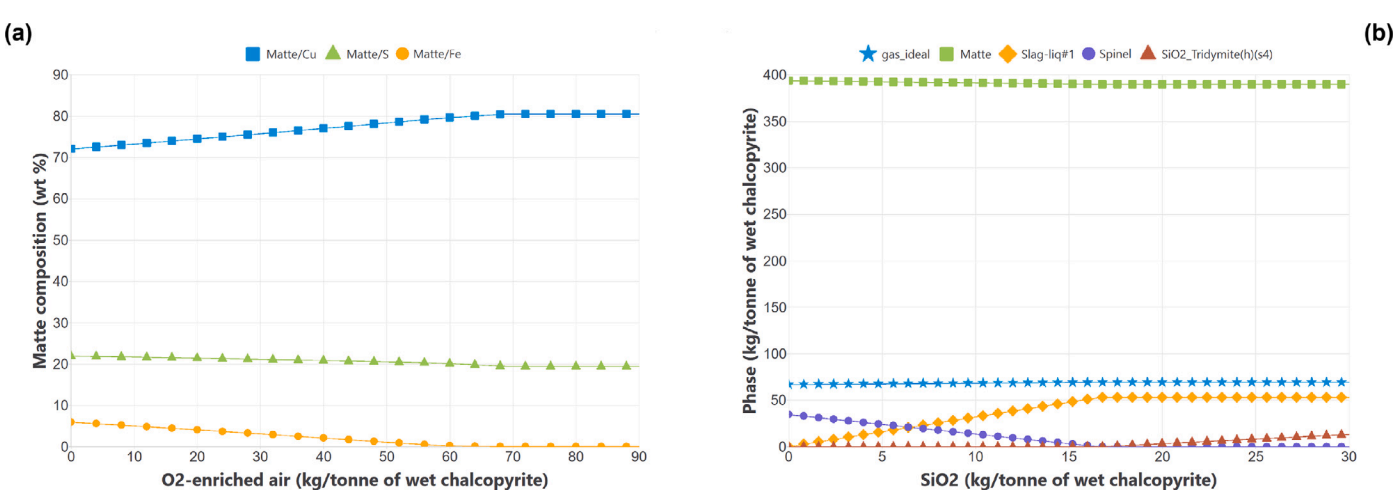


**Fig. 9.** (a) Matte composition evolution upon $O_2$-enriched air additions (x-axis) for the *slag-forming* step. (b) phase assemblage evolution for the *slag-forming* step as a function of the $SiO_2$ added to the reactor using 60 kg of injected air.

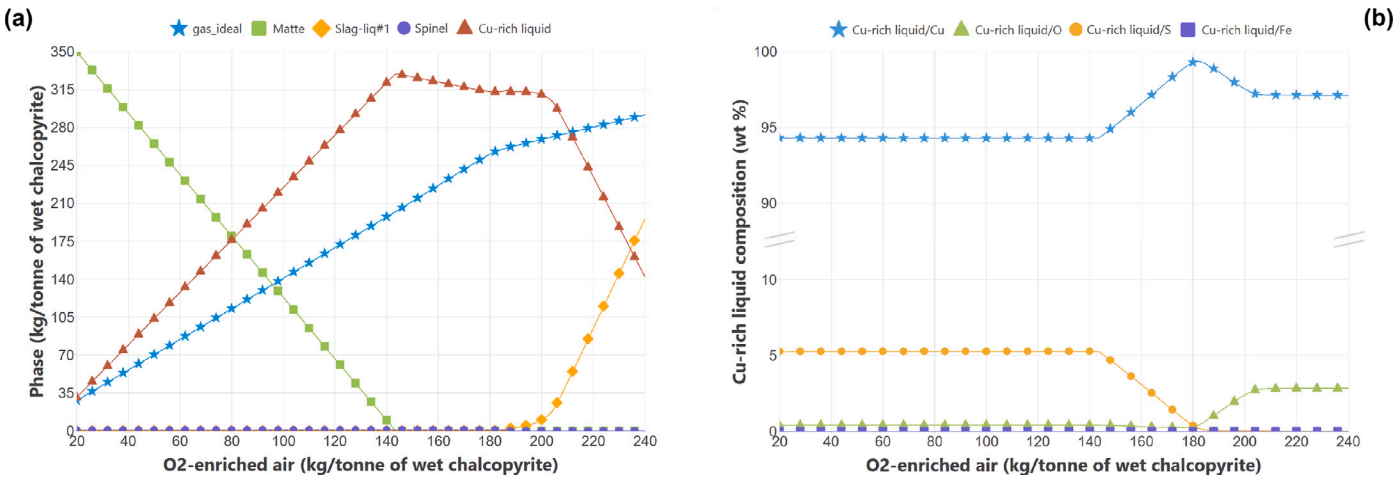


**Fig. 10.** (a) Phase assemblage evolution during the copper-making step (converter 2) as a function of the air injection. (b) Composition of the produced liquid copper solution as a function of the air injection in converter 2.

transferred to the slag phase in the first metallurgical operation (*i.e.*, smelting as shown in Fig. 11). Also, the majority of Pb is separated during smelting through the slag, molten metal phase and gas phase, with volatile species including PbS($g$), Pb($g$), PbO($g$), PbH($g$) and $Pb_2$($g$). Although around 23.6 wt% of Pb remains in the matte phase, continuous transfer to the slag phase occurs during the slag-forming step. Hence, only 6.2 wt% of the original Pb remains in the final Cu-rich molten metal phase (blister copper) exiting the copper-making unit (Fig. 11). In the case of Fe, it is effectively removed via the slag phase (Fig. 11).

Regarding silver (Ag), it is challenging to remove from E-waste during recycling due to its affinity for the matte and molten metal phases involved in copper production. According to our simulation, 99.8 wt% of the original Ag is found in the final Cu-rich molten alloy (Fig. 11). To address this concern, Faraji et al. [59] propose Ag removal from blister copper through subsequent electro-refining operations which ultimately transfer it in the form of anode slime along with gold (Au) and platinum group metals (PGMs) to be further processed and valorized.

As for nickel (Ni), it is evident that this metal is also challenging to separate, with up to 59.3 wt% of the initial quantity found in blister copper (Fig. 11). Nevertheless, the initial nickel content in the scrap is only 0.03 wt% (Table 4). The final Ni concentration is therefore small.

### 3.3. Ti primary metal production from rutile ($TiO_2$)

Titanium alloys are standard materials employed in aerospace engineering, specifically for the construction of aircraft engines and landing gear. This is due to their exceptional corrosion resistance and good specific mechanical properties [60]. Remarkably, titanium alloys can be half the weight of equivalent steels and Ni-based superalloys [61]. The chemical industry also uses a lot of titanium alloys, mainly for applications dealing with oxidizing acids, for which a high corrosion resistance is required [62].

The most common titanium-rich minerals that are industrially processed for the production of titanium are ilmenite-based (~40%–65% $TiO_2$ content) and rutile-based (~95% $TiO_2$ content) ores [63,64]. Ilmenite represented about 91% of the world's offer for titanium minerals in 2011. Other significant titanium sources include anatase-based and brookite-based ores among others [64]. As reported by the *National Minerals Information Center from the United States Geological Survey* (USGS), the four main ilmenite-ore producers in 2019 were China, South Africa, Canada and Australia [65]. Due to the large reserves of ilmenite-based ores around the globe, they will act as the main source for titanium production for several years to come [64]. On the other hand, rutile ore deposits are typically much less abundant in nature and are becoming difficult to find. Synthetic rutile can be synthesized from ilmenite ores by eliminating iron oxides and other impurities via pyrometallurgical and hydrometallurgical processes [66]. The Rio Tinto QIT electric-arc reduction furnace which processes ilmenite-concentrate to produce clean pig iron (*i.e.*, carbon-saturated iron which contains a low concentration of phosphorus and sulfur) and $TiO_2$-rich slag (which is solidified and further processed to obtain pure $TiO_2$) is an example of such a process. Synthetic rutile usually reaches a concentration of around 92% of $TiO_2$ [64].

#### 3.3.1. Exploration of the potential carbo-reduction of $TiO_2$

According to the Ellingham diagram (refer to the Appendix of Part 1 [13]), Ti can theoretically be extracted from rutile by directly reducing it using carbon under standard conditions via the following reaction:

$$TiO_2(s) + 2C(s) \rightarrow Ti(l) + 2CO(g) \tag{12}$$

A preliminary calculation performed with the *Reaction* module of FactSage under standard conditions suggests that this endothermic reaction is thermodynamically favorable at temperatures above 2040.39 K (temperature obtained by imposing $\Delta G^0$=0). This theoretical high temperature would lead to refractory material selection challenges, especially considering that liquid titanium would be produced under these conditions (reaction (12)). An alternative strategy to extract titanium at lower temperatures is to substantially reduce the operating pressure of the unit. The targeted temperature of the process can then be lowered below the melting point of titanium (*i.e.*, 1941 K) to further limit the wear of the refractory lining used in the furnace. In this alternative scenario, a hypothetical operational temperature of 1400 K is imposed to the system. A CO partial pressure below 7e-5 bar is required for reaction (13) to proceed. This stringent vacuum condition would be difficult to apply in practice.

$$TiO_2(s) + 2C(s) \rightarrow Ti(s) + 2CO(g) \tag{13}$$

These two sets of operating conditions would be valid if reactions (12) and (13) were the only reaction pathways to occur. However, this thermodynamic analysis is incomplete and oversimplified. When considering the potential formation of all the phases available in the FactSage databases, it is found that the single use of carbon as a cheap reducing agent leads to the formation of titanium carbide (TiC), a

**Table 3**
Final simulation parameters and results for Cu production considering 1 tonne of wet chalcopyrite as the calculation basis.

| Unit | Inputs | Output phases | Phase composition | Literature |
|---|---|---|---|---|
| Smelting<br>1250 °C, 2.6 bar<br>ΔH = −271 MJ | • 1 tonne of chalcopyrite (8 wt% $H_2O$)<br>• 100 kg of $SiO_2$ | 435.19 kg of matte | 72.07 wt% Cu<br>5.96 wt% Fe<br>21.97 wt% S | 71–72 wt% Cu[a]<br>3–5 wt% Fe[a] |
| | • 680 kg of 40 mol% $O_2$ air | 442.31 kg of slag* | 57.43 wt% Fe<br>29.65 wt% O<br>10.57 wt% Si<br>1.24 wt% S<br>1.11 wt% Cu | 3–4 wt% Cu[b] |
| | | 25.05 kmol of gas | 55.00 mol% $N_2$<br>27.06 mol% $SO_2$<br>17.44 mol% $H_2O$<br>0.24 mol% $H_2$<br>0.11 mol% $S_2$<br>Other species | 15–20 Vol.% $SO_2$ (wet)[c] |
| Slag-forming<br>(Converter 1)<br>1250 °C, 2.6 bar<br>ΔH = −137 MJ | • 435.19 kg of matte from smelting<br>• 17 kg of $SiO_2$<br>• 60 kg 40 mol% $O_2$ air | 389.80 kg of matte (mainly *white metal*) | 79.84 wt% Cu<br>20.01 wt% S<br>0.15 wt% Fe | ~1 wt% Fe[d] |
| | | 52.96 kg of slag** | 47.83 wt% Fe<br>32.71 wt% O<br>14.81 wt% Si<br>4.59 wt% Cu<br>0.06 wt% S | |
| | | 1.76 kmol of gas | 68.90 mol% $N_2$<br>31.08 mol% $SO_2$<br>0.02 mol% SO<br>Other species | 20 Vol.% $SO_2$[e] |
| | | 0.22 kg of $SiO_2$ (Tridymite) | | |
| Copper-making<br>(Converter 2)<br>1250 °C, 2.6 bar<br>ΔH = −241 MJ | • 389.80 kg of matte from converter 1<br>• 170 kg of 40 mol% $O_2$ air | 317.42 kg of Cu-rich liq. | 98.04 wt% Cu<br>1.69 wt% S<br>0.26 wt% O<br>0.00 wt% Fe | 98 wt% Cu[e]<br>1.3 wt% S[e] |
| | | 0.83 kg of spinel | 71.56 wt% Fe<br>27.62 wt% O<br>0.82 wt% Cu | |
| | | 5.71 kmol of gas | 60.34 mol% N2<br>39.65 mol% $SO_2$<br>0.01 mol% SO<br>Other species | 20 Vol.% $SO_2$[e] |

*Phase constituents: 58.00 wt% FeO, 22.15 wt% $SiO_2$, 15.97 wt% $Fe_2O_3$, 1.22 wt% $Cu_2O$, 0.71 wt% $SiS_2$ and 0.44 wt% $Fe_2S_3$.
**Phase constituents: 47.23 wt% FeO, 31.66 wt% $SiO_2$, 31.66 wt% $SiO_2$, 15.83 wt% $Fe_2O_3$ and 5.17 wt% $Cu_2O$.
[a] [a]Output matte composition from Noranda Smelting Furnace, Canada [47].
[b] [b]Output slag composition from Noranda Smelting Furnace, Canada [47].
[c] [c]Output gas composition from Noranda Smelting Furnace, Canada [47].
[d] [d]Fe content after *slag-forming* step [47].
[e] [e]Xstrata Copper Horne Smelter [47].

**Table 4**
Metallic composition in E-waste targeted from portable audio scrap for recycling. Data sourced from [58], exclusively considering elements with concentrations ≥ 100 ppm.

| Composition (wt%) | | | | | | |
|---|---|---|---|---|---|---|
| Cu | Al | Pb | Fe | Ni | Ag | Balance |
| 21 | 1 | 0.14 | 23 | 0.03 | 0.015 | Not reported in [58] (approximated to C-graphite in this work) |

compound known for its undesirable brittleness [67]. For instance, Fig. 12 illustrates the phase assemblage results of 1 mol of $TiO_2$ reacted with a variable amount of carbon in the form of graphite (x-axis) at 2045 K and 1 bar, indicating the presence of titanium carbide (FCC-A1 phase, symbolized in green).

In Fig. 12, three different scenarios can be explored with respect to the stoichiometric reaction (12): (1) Carbon deficiency: <2 mol of C/mol of $TiO_2$, (2) Stoichiometric amount: 2 mol of C/mol of $TiO_2$, and (3) Excess of carbon >2 mol of C/mol of $TiO_2$. For carbon-deficient reducing conditions at 2045 K and 1 bar, Ti is firstly reduced from $Ti^{4+}$ (in Rutile) to $Ti^{3+}$ and transferred into a $TiO_2$-$Ti_2O_3$ slag phase (orange line). **Figure E1** (**Electronic Supplementary Material**) shows that the liquidus temperature of the slag phase is lowered upon the partial reduction of $Ti^{4+}$ to $Ti^{3+}$. At carbon additions of about 0.4 mol/mol of $TiO_2$, titanium carbide starts forming (FCC-A1 phase illustrated in green). Under these conditions, titanium is partitioned between this carbide solid solution and the slag phase. At the stoichiometric ratio (*i.e.*, 2 mol of C/mol of $TiO_2$), there is still a substantial quantity of non-fully reduced titanium in the slag phase. Above the addition of 2.8 moles of C/mole of $TiO_2$, the slag phase does not appear anymore and all the Ti is contained in the carbide phase (FCC-A1). Therefore, it is not possible to produce liquid Ti through direct reduction with carbon under these conditions.

A similar series of thermodynamic calculations were carried out for the set of operating conditions that were believed to conduct the production of solid Ti via reaction (13), *i.e.*, 1400 K and 7e-5 bar. Equivalently, Ti in the ore is partially reduced by adding C and leads to the formation of multiple Ti-oxide phases as shown in Fig. 13. Finally, the formation of titanium carbide arises from the reaction between $Ti_2O_3$ and C for carbon additions > 0.5 mol of C/mol of $TiO_2$. These

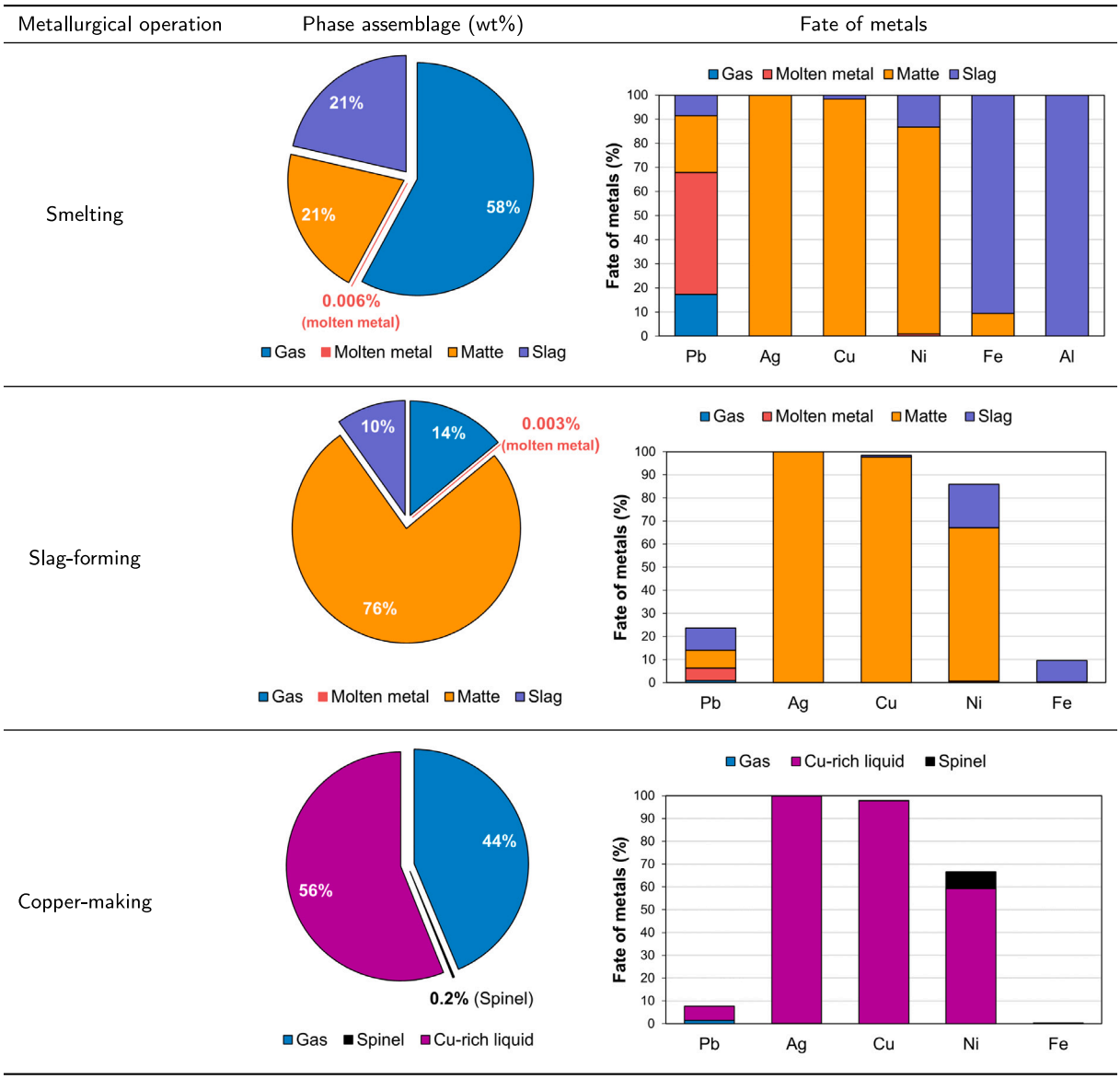


**Fig. 11.** Phase assemblage evolution and fate of metals in copper production from wet chalcopyrite with 10 wt% of scrap (Table 4) recycling in a 1-tonne feedstock basis. Operations include: (1) Smelting at 1250 °C and 2.6 bar (with 940 kg of 40 vol.%-$O_2$ air and 100 kg of $SiO_2$ to achieve 72 wt% of Cu in matte), (2) Slag-forming at 1300 °C and 2.6 bar (with 60 kg of 40 vol.%-$O_2$ air and 13 kg of $SiO_2$ to achieve 80 wt% of Cu in matte) and (3) Copper-making at 1300 °C and 2.6 bar (with 170 kg of 40 vol.%-$O_2$ air injection to obtain 99 wt% of Cu in the molten metal phase).

thermodynamic simulations clearly show that C has a high affinity with Ti resulting in the production of titanium carbide, which makes the carbo-reduction an inadequate strategy for the production of metallic Ti.

### 3.3.2. *Carbo-chlorination roasting*

To address the challenges associated with the formation of titanium carbides, as discussed in Section 3.3.1 (direct carbo reduction), alternative reactants such as chlorine can be incorporated in conjunction with carbon, leading to a technique known as carbo-chlorination roasting [68]. In this approach, $TiO_2$ is transformed into gaseous titanium chloride via the following reaction [69]:

$$TiO_2(s) + 2Cl_2(g) + C(s) \rightarrow TiCl_4(g) + CO_2(g) \quad (14)$$

This roasting operation also allows the efficient separation of some impurities (such as $SiO_2$, MgO and CaO) from the produced chlorides. For rutile, the carbo-chlorination roasting is industrially carried out at 1273 K [69,70] into a fluidized bed reactor which is called a chlorinator (Fig. 14). Table 5 reports the simulation results of reacting 1 mol of $TiO_2$ with stoichiometric amounts of C and $Cl_2$ (according to reaction (14)) at 1273 K. FactFlow predicts the formation of a gas phase containing ~1 mol of $TiCl_4$ and ~1 mol $CO_2$ in the carbo-chlorination reactor along with minor traces of CO($g$), $Cl_2$($g$) and Cl($g$). The separation of the dust from the gas stream exiting the chlorinator is portrayed in Fig. 14a, where a cyclone is employed for this purpose. In this work (Table 5), this physical separation is represented by the splitter node in FactFlow separating the unreacted Rutile, as illustrated in Fig. 14b.

### 3.3.3. *Condensation and purification of $TiCl_4$*

As outlined in Section 3.3.2, the gas mixture emerging from the chlorinator primarily contains $TCl_4$ and $CO_2$ at a temperature of 1273 K. In the industrial Kroll process, this gas mixture undergoes an initial treatment in a cyclone for the removal of solid particles. Subsequently, it passes through a condenser aimed at liquefying $TiCl_4$, thereby facilitating the separation of $CO_2$ and CO gaseous species (Fig. 14). Adjusting

**Table 5**
Simulation inputs and outputs for Ti production considering a calculation basis of 1 mol of Rutile ($TiO_2$).

| Unit | Inputs | Output phases | Phase composition |
|---|---|---|---|
| Carbo-chlorinator<br>1273 K, 1 bar | 1 mol of $TiO_2$<br>1 mol of C<br>2 mol of $Cl_2$ | 2.003 mol of gas | 49.82 mol% $TiCl_4$<br>49.72 mol% $CO_2$<br>0.22 mol% CO<br>0.20 mol% $Cl_2$<br>0.04 mol% Cl<br>Other minor species |
| | | 0.002 mol of Rutile | ~100 mol% $TiO_2$ |
| Condenser<br>300 K, 1 bar | Gas phase from carbo-chlorinator | 1.017 mol of gas | 98.15 mol% of $CO_2$<br>1.64 mol% of $TiCl_4$<br>0.21 mol% of $CCl_4$<br>Other minor species |
| | | 0.981 mol of liquid $TiCl_4$ | Pure substance |
| | | 1.8 x$10^{-7}$ mol of graphite | Pure substance |
| Evaporation (and distillation) | $TiCl_4(l)$ and C($s$) | 0.981 mol of $TiCl_4(g)$ | 100 mol% $TiCl_4$ |
| 450 K, 1 bar | from condenser | 1.8 x$10^{-7}$ mol of C($s$) | Pure substance |
| Magnesiothermic reduction<br>1100 K, 1 bar | $TiCl_4(g)$ from evaporation<br>2 mol of Mg | 0.983 mol HCP-A3 phase | 99.84 wt% Ti<br>0.16 wt% Mg |
| | | 1.962 mol of $MgCl_2$ | Pure substance |
| | | 0.036 mol of liquid phase | 99.98 wt% Mg<br>0.02 wt% Ti |
| Vacuum distillation<br>1273 K, 0.01 bar | Ti($s$), $MgCl_2(l)$ and Mg($l$) from reduction | 0.966 mol of BCC-A2 phase | 100 wt% Ti<br>5.7 × $10^{-4}$ wt% Mg |
| | | 1.986 mol of gas | 94.67 mol% $MgCl_2$<br>2.97 mol% Mg<br>1.49 mol% $(MgCl_2)_2$<br>0.67 mol% $TiCl_3$<br>0.11 mol% $TiCl_2$<br>0.08 mol% MgCl |

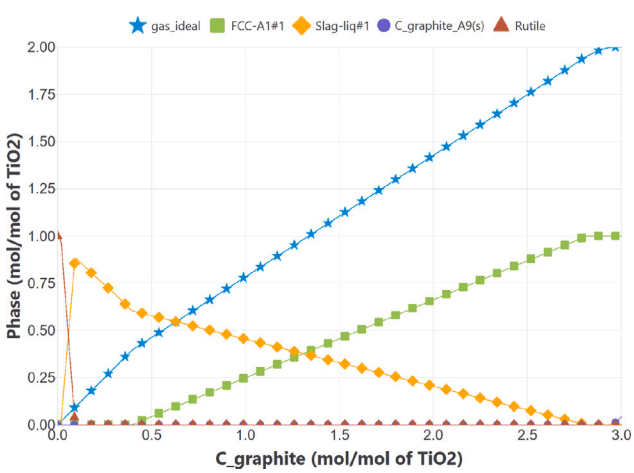


**Fig. 12.** Simulation results of 1 mol of $TiO_2$ reacted with a variable amount of C_graphite at 2045 K and 1 bar.

the condenser temperature yields Fig. 15, illustrating the evolution of gaseous $TiCl_4$ and the appearance of liquid $TiCl_4$. This graph indicates the initiation of liquefaction around 480 K. Assuming the condenser can achieve temperatures as low as 300 K, the resulting outputs consist of a $CO_2$-rich gas phase, along with liquid $TiCl_4(l)$ and graphite (refer to Table 5 for detailed composition information).

In this work, the condensed phases exiting the condenser are only $TiCl_4(l)$ and C($s$); thus, carbon removal is performed by directing these phases through an evaporator (Fig. 14) strategically set just above the boiling point of $TiCl_4$ (Table 5). In the industrial Kroll process, specialized units use evaporation and distillation to remove impurities like $FeCl_x$, $AlCl_3$, $VOCl_3$ (reduced to $VCl_4$ with $H_2S$), $SnCl_4$, and $SiCl_4$ [69]. This purification strategy ensures the meticulous elimination of impurities, guaranteeing the production of high-purity $TiCl_4$ that is sent later to the Magnesiothermic reduction unit (Fig. 14).

### 3.3.4. *Magnesiothermic reduction of $TiCl_4$*

The purified $TiCl_4$ gas, originally obtained through carbo-chlorination roasting, undergoes subsequent treatment through a magnesiothermic reduction process (Fig. 14). The primary objective of this procedure is to transfer chlorine, chemically bound to titanium, onto magnesium through the following reaction:

$$TiCl_4(g) + 2Mg(l) \rightarrow 2MgCl_2(l) + Ti(s) \quad (15)$$

This chemical transformation represents a crucial step in the overall synthesis, with magnesium serving as the reducing agent to produce liquid magnesium chloride ($MgCl_2$) and solid titanium (Ti) at 1100 K in the industrial Kroll process [69].

Fig. 16 shows the predicted phase assemblage evolution as a result of the magnesiothermic reaction of 0.983 mol of pure $TiCl_4$ (*i.e.*, after its condensation and distillation). Two scenarios are explored on this figure as liquid $MgCl_2$ can dissolve $TiCl_2$ in this temperature range [71]. In scenario #1 (solid lines), the magnesiothermic reduction is performed using the available FactSage databases which do not consider the potential formation of the $MgCl_2$-$TiCl_2$ liquid solution. In scenario #2 (dot lines), it is assumed that an ideal solution between $MgCl_2$ and $TiCl_2$ can form (the ideal solution was created in FactSage and then imported into FactFlow via a CST file). As it can be seen on this figure, accounting for the potential presence of the liquid $MgCl_2$-$TiCl_2$ solution does not have a major impact on the final product obtained with this process (blue lines). In both scenarios, the HCP solid solution mostly contains Ti with a minor amount of Mg at the stoichiometric addition of Mg. The main difference between these two scenarios is the transfer of Ti to the $MgCl_2$-$TiCl_2$ liquid solution during the reduction process.

Table 5 provides the composition of the Ti-HCP product obtained through the reaction of 0.981 mol of pure $TiCl_4$ and 2 mol of excess Mg. The results reveal a high-purity titanium product along with an

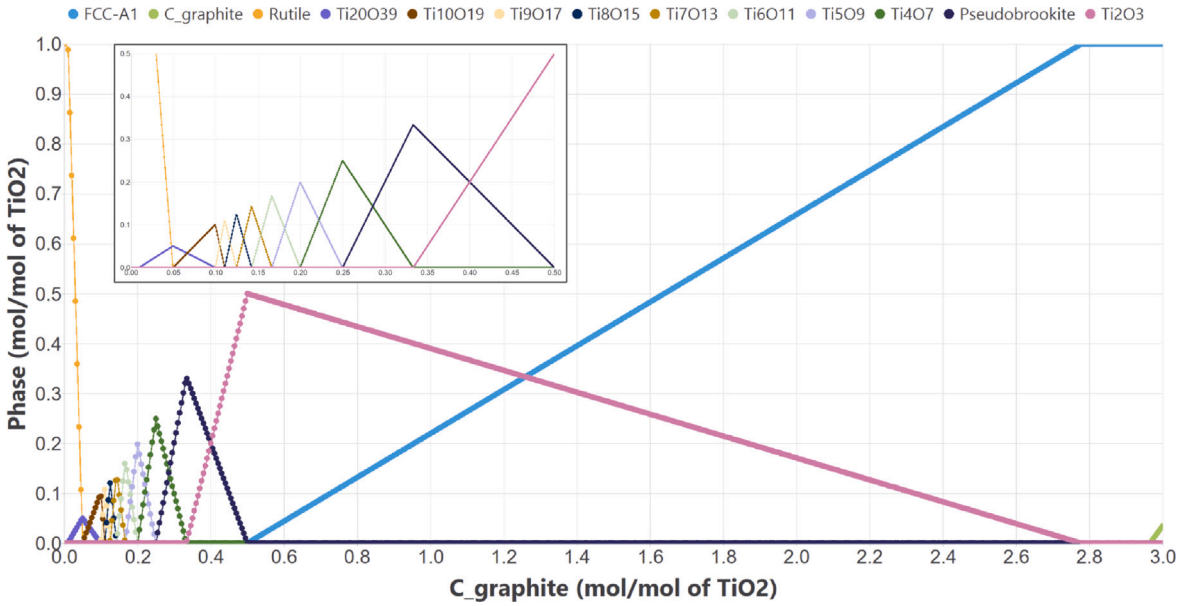


**Fig. 13.** Simulation results of 1 mol of $TiO_2$ reacted with a variable amount of C_graphite at 1400 K and 7 Pa.

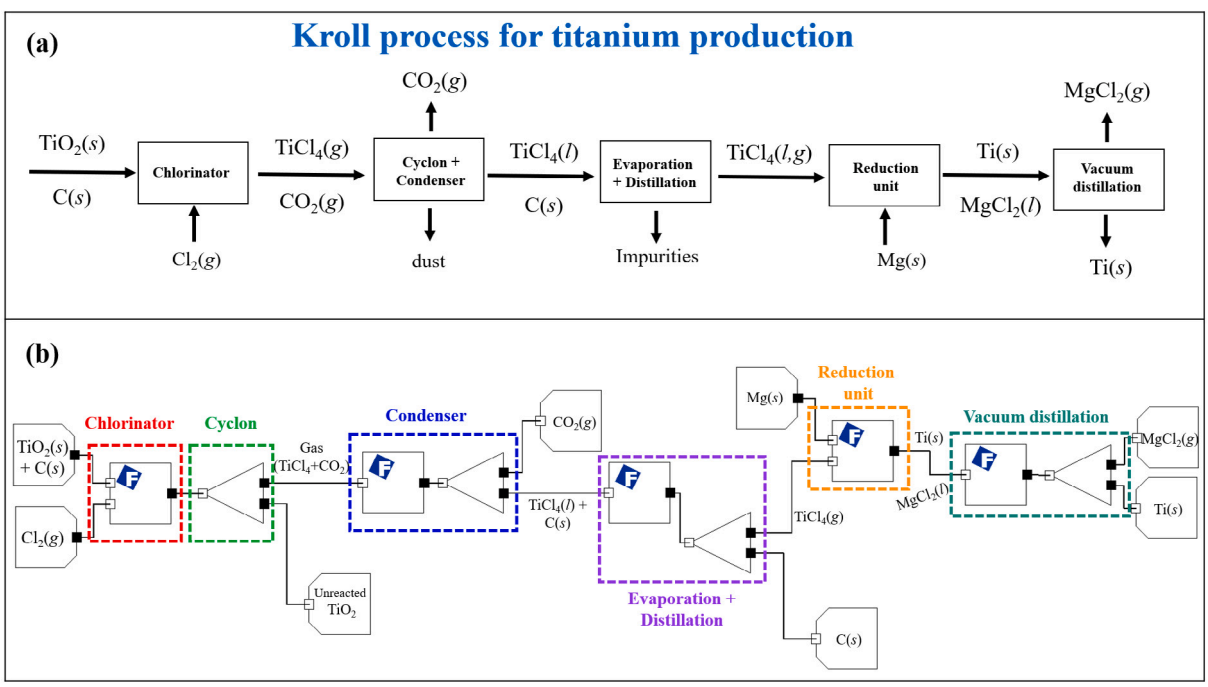


**Fig. 14.** (a) Summary of the Kroll process for titanium production from rutile. (b) Flowsheet of the Kroll process in FactFlow, highlighting the different unit operations required to treat the titanium ore.

excess of $MgCl_2$ and liquid Mg. The miscibility gap between Ti and Mg, as shown in the Mg-Ti phase diagram (**Figure E2** in the **Electronic Supplementary Material**), supports the choice of Mg for this process. This gap ensures that, whether the targeted Ti-rich phase is solid or liquid, Ti and Mg remain immiscible, yielding a high-purity Ti product. As reported in the literature, solid titanium produced in this process is porous and may contain liquid $MgCl_2$ in its open pores [69]. An efficient way to remove this liquid chloride from the system is to perform a vacuum heating of the Ti sponge at 1273 K and 0.1–1 Pa [69]. In this work, the vacuum distillation step is represented by directing the reduction outputs to another FactFlow reactor node, as shown in Fig. 14. As indicated in Table 5, operating the distillation chamber at 1273 K and 0.1 bar results in the complete vaporization of $MgCl_2$ and Mg. This leads to the production of a clean titanium sponge, effectively removing undesirable liquid chlorides from the system. It is worth mentioning that the vacuum conditions are less demanding if an argon atmosphere is imposed on the system. Such an example was for instance reported in part 1 of this series of articles [13].

Overall, five distinct steps were identified to produce metallic titanium from rutile via a series of thermodynamic simulations: (1) carbo-chlorination of rutile, (2) gas condensation, (3) liquid $TiCl_4$ evaporation/distillation, (4) magnesiothermic reduction and (5) vacuum distillation. This theoretical framework is subject to comparative analysis with the Hunter and Kroll processes, which represent the predominant existing methodologies for titanium production [68]. Both the Hunter and Kroll processes share a parallel procedure involving

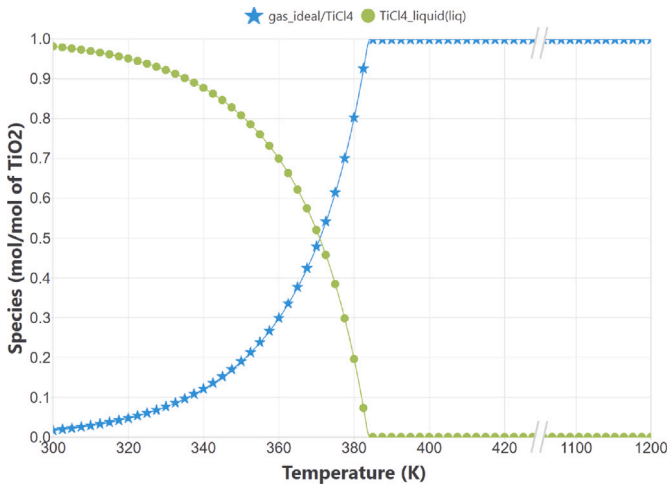


**Fig. 15.** $TiCl_4$ liquefaction curve.

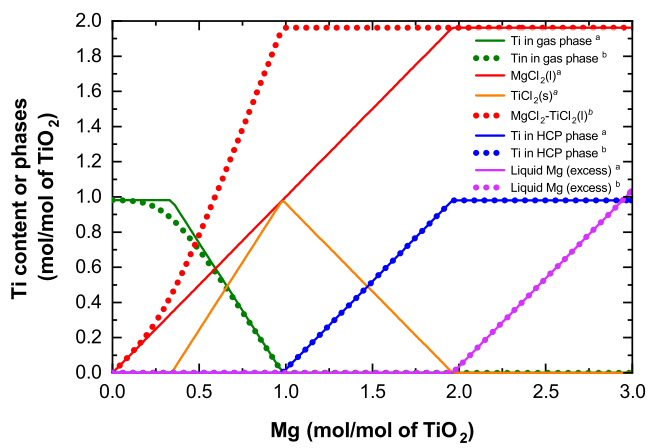


**Fig. 16.** Predicted titanium partitioning in selected phases during the magnesiothermic reduction of pure $TiCl_4$ (from evaporation) as a function of the Mg additions in the system.
[a]Without ideal $MgCl_2$-$TiCl_2$ liquid solution.
[b]With ideal $MgCl_2$-$TiCl_2$ liquid solution.

the production of $TiCl_4$; the key distinction lies in the choice of the reducing agent for Cl removal, with magnesium employed in the Kroll process and sodium in the Hunter process [72].

### 3.4. MIDREX process modeling through stream recycling and bypass

MIDREX is a well-established primary steel production process to produce direct reduced iron (DRI) pellets using a counter-flow solid-gas shaft furnace [73]. This industrial process involves feeding hematite-rich pellets into the shaft furnace, along with the injection of syngas (obtained from the reforming of natural gas) which acts as the reducing agent to produce the metallized DRI pellets. Given that the steel industry contributes to about 7% of the total anthropogenic $CO_2$ emissions [74,75], there is currently a significant interest in the potential substitution of natural gas by green hydrogen to lower the greenhouse gas emissions of the process [76]. This change in the $H_2/CO$ ratio may also have profound implications on the metallization of the DRI pellets, on the overall energy balance of the shaft furnace, on the water removal of the process gas via the scrubbers, and on the excess hydrogen management (which is thermodynamically required to allow the complete reduction of the oxide pellets). All these theoretical impacts can be evaluated from a CT-based process flowsheet.

**Table 6**
Input gas composition (% vol.) for the reformer unit, data retrieved from Bond et al. [78].

| $H_2$ | $CH_4$ | CO | $CO_2$ | $H_2O$ | $N_2$ | $C_2H_6$ |
|---|---|---|---|---|---|---|
| 37.42 | 18.34 | 17.77 | 15.09 | 8.97 | 2.15 | 0.26 |

The process flowchart used to model the MIDREX process using FactFlow is presented in Fig. 17. This figure illustrates the various unit operations and virtual reactors which are required to model this process. These include (i) a reformer, (ii) an enrichment unit, (iii) the reduction furnace, (iv) a scrubber and (v) a burner unit. All units are interconnected through recycling loops, which ultimately allow the representation of the entire MIDREX process. This last example summarizes all the functionalities currently available in FactFlow to simulate pyrometallurgical processes.

#### 3.4.1. Approximation of steam methane reforming (SMR) kinetics via stream bypass

In the MIDREX process, the syngas used in the reduction furnace is obtained through natural gas reforming and consists mainly of hydrogen ($H_2$) and carbon monoxide (CO). The MIDREX configuration enables the recycling of the $CO_2$-rich top-gas exiting the reduction furnace (red section in Fig. 17), using it as a feed reactant into the reforming unit (orange section in Fig. 17). The scrubber (blue section in Fig. 17) between the furnace and the reformer is used to remove excess water vapor from the gas exiting the furnace. The reformer is composed of super-alloy steel tubes filled with nickel/alumina catalysts [77], where the production of $CO(g)$ and $H_2(g)$ takes place via the following reactions mainly:

$$CH_4(g) + H_2O(g) \longrightarrow CO(g) + 3H_2(g) \qquad \Delta H_{950°C,1.5atm} = +227.32\ \text{kJ} \tag{16}$$

$$CH_4(g) + CO_2(g) \longrightarrow 2CO(g) + 2H_2(g) \qquad \Delta H_{950°C,1.5atm} = +259.92\ \text{kJ} \tag{17}$$

The kinetics of these chemical reactions are inherently slow, which explains the presence of catalysts inside the reforming tubes. In order to match the kinetics occurring in the reformer (orange section in Fig. 17), a bypass stream of unreacted gas (comparable to the application of virtual species in FactSage, as detailed in the recent work of Pelton et al. [40]) can be incorporated into the FactFlow modeling. This facilitates the modulation of reformer outputs by means of a bypass factor ($\gamma$), as follows:

$$[\text{Reacted gas}] = (1-\gamma) \times [\text{Entry gas}] \tag{18}$$

$$[\text{Unreacted gas}] = (\gamma) \times [\text{Entry gas}] \tag{19}$$

Where [Reacted gas] is the output after an equilibrium calculation, [Unreacted gas] represents the bypass stream and [Entry gas] is the gas mixture entering the reforming unit (orange section in Fig. 17). A typical composition (% vol.) of the gas entering the reforming unit is reported in Table 6. Note that a *Mixer* node was added at the end of the reforming section, which calculates the enthalpy change to bring both [Reacted gas] (exiting the reactor) and [Unreacted gas] streams to the same specified temperature and pressure before entering the enrichment unit (green section in Fig. 17). This is particularly important because it ensures that the energetics of the unreacted gas are included in the overall energy balance, despite being ignored in the reaction within the reforming section.

The error associated with the stream bypass was determined as the mean difference between the gas composition calculated in FactFlow and the values reported by Bond et al. [78], using the following expression:

$$error = \frac{\sum_{i=1}^{5} |Y_i^{ref} - Y_i|}{5} \tag{20}$$

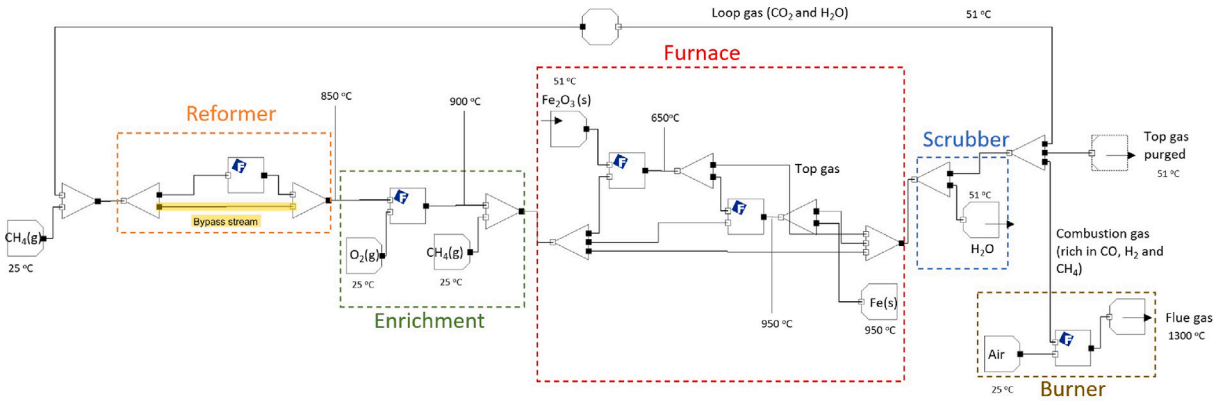


**Fig. 17.** FactFlow process modeling of the MIDREX process, highlighting various unit operations within the system with a calculation basis of 309.3 tonne of hematite pellets.

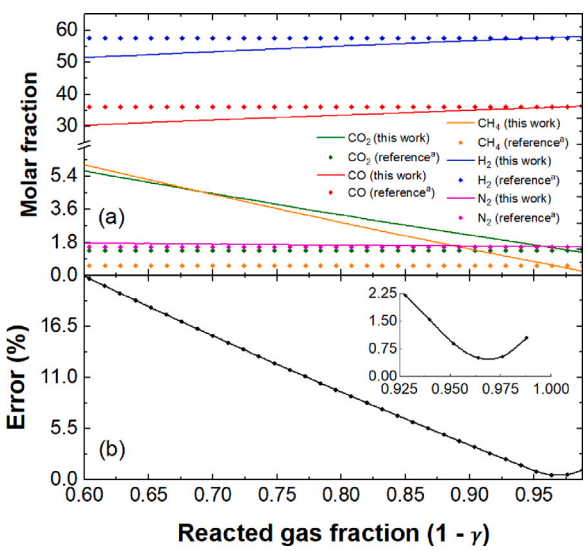


**Fig. 18.** (a) Output reforming gas composition (solid lines) as a function of the bypass factor, compared to the experimental values reported by [a]Bond et al. [78] (dotted lines). (b) Modeling error (Eq. (20)) as a function of the bypass factor.

where $Y_i$ is molar fraction of the $i$ species in the output gas (*i.e.*, CO, $H_2$, $CO_2$, $H_2O$ and $CH_4$) and $Y_i^{ref}$ are the industrial values reported by Bond et al. [78].

Fig. 18a shows the evolution of the concentration of the major gaseous species which exit the reforming unit in FactFlow as a function of (1-$\gamma$) to control the extent of the reforming reactions. According to this figure, the optimum bypass factor to mimic the reaction kinetics is $\gamma = 0.036$. The error associated with the molar fraction of the gas species is presented in Fig. 18b. Analogous to Fig. 18a, it suggests that 0.964 is the optimal setting for (1-$\gamma$) to capture the reaction kinetics of the reformer. This value can also be considered as the reformer efficiency.

### 3.4.2. MIDREX furnace modeling

In the MIDREX furnace, iron oxide pellets (mainly containing hematite grains) react with a counter current of syngas, leading to the formation of metallic iron via the following reactions:

$$Fe_2O_3(s) + 3CO(g) \longrightarrow 2Fe(s) + 3CO_2(g) \qquad \Delta H_{900°C,1.5atm} = -36.8\ \text{kJ} \tag{21}$$

$$Fe_2O_3(s) + 3H_2(g) \longrightarrow 2Fe(s) + 3H_2O(g) \qquad \Delta H_{900°C,1.5atm} = +62.4\ \text{kJ} \tag{22}$$

In FactFlow, the furnace is approximated using two interconnected equilibrium reactors, as highlighted by the red rectangle in Fig. 17. One reactor operates at a temperature of 650 °C, simulating the upper part of the furnace, while the second, operating at 950 °C, represents the lower part. The first stream connection between the reactors is essential for enabling the upward flow of gas and its reaction with freshly introduced hematite. The second connection involves a loop stream that transfers partially reduced pellets from the top to the bottom of the furnace. Therefore, upon injecting hematite pellets into the furnace, they undergo a two-stage reaction sequence: first in the upper equilibrium reactor and subsequently again in the lower equilibrium reactor fed with syngas. We acknowledge that another approach to modeling the furnace could be the merging of multiple adiabatic reactors, in which the individual temperature of each sub-reactor is established by the heat balance from the quantity of injected hot reducing gases and the energy released from reaction (21), which together compensate for the heating and endothermic reduction of $Fe_2O_3$ (reaction (22)). In our current study, however, we present a simplified version with only two interconnected reactors operating at imposed temperatures.

Table 7 presents the metallization degree as well as the direct $CO_2$ emissions from the simulated MIDREX process flowsheet for two operating condition scenarios. In the first scenario, only natural gas is injected in the process, which is similar to the operating conditions presented by Bond et al. [78]. In scenario 2, 5% (vol.) of natural gas is replaced by hydrogen. The metallization is defined here as the mass ratio of metallic iron present in the DRI pellets over the total amount of Fe in the pellets, *i.e.*:

$$\text{Metallization} = \frac{m_{Fe}^{metal-DRI}}{m_{Fe}^{total}} \tag{23}$$

Our simulation results are compared to the data reported by Bond et al. [78]. Both the grade of DRI pellets and the direct $CO_2$ emissions are consistent with the values reported by these authors. The natural gas input for the base case (scenario 1) is 183.3 $Nm^3$/tonnes of DRI. This table shows that the substitution of 5% of natural gas by $H_2$ decreases the $CO_2$ emissions from 426 to 414 kg/tonne DRI while reducing the product quality (*i.e.*, a lower metallization).

## 4. Conclusion

Four complex pyrometallurgical processes modeled using computational thermochemistry were presented in this work. They were specifically chosen to demonstrate how computational thermochemistry can be used to solve overall mass and energy balances for processes involving many unit operations and streams. An indirect way to account for reaction kinetics which requires plant data using virtual bypasses was also presented. A new graphical interface called FactFlow which is now integrated into FactSage provides an intuitive interface for creating

**Table 7**
Iron concentration in reduced pellets and $CO_2$ emissions from the simulated MIDREX process, compared to the data reported by Bond et al. [78]. "Scenario 1" refers to a simulation performed considering similar operating conditions as Bond et al. [78]. "Scenario 2" refers to a simulation with 5% of the natural gas replaced by $H_2$.

| | Scenario 1 (Base case) | Scenario 2 5% $H_2$ | Literature [78] |
|---|---|---|---|
| Metallization | 95.8 | 92.8 | 91.9 |
| $CO_2$ emissions (kg/tonnes DRI) | 426 | 414 | 393 |

such processes using modular nodes. Key takeaways from these process simulations, apart from the overall excellent agreement between the available data and predicted ones for each explored process, are as follows:

- **Production of ferrosilicon via two-stage virtual reactor zones**
  The smelting of quartzite in a submerged arc furnace to produce the FeSi75 alloy can be represented using a two-stage furnace. The upper virtual equilibrium reactor is intended to model the lower temperature (*i.e.*, 1665 °C) of the furnace while the bottom virtual equilibrium reactor represents the high temperature (*i.e.*, 1935 °C) zone. A recycling loop to transfer the gas evolving from the bottom of the furnace to the upper part is required. The importance of defining an objective convergence criterion by analyzing all phase amounts in a system was demonstrated.
- **Cu primary metal production from chalcopyrite and E-waste**
  The Noranda-like process which allows the extraction of copper from chalcopyrite was explored. The complete process flowsheet included (i) smelting, (ii) *slag-forming* and (iii) *copper-making* sequential stages. This example clearly demonstrated the analysis process which is required to determine the optimal conditions for each unit operation using graphical results. This analysis process included the evaluation of the optimal amount of $O_2$-enriched air for each unit operation as well as the amount of silica to be added during the smelting process and the slag-forming stage. Phase assemblage, matte composition, as well as metal purity were used as indicators to quantify the efficiency of each process. Finally, the fate of metals such as Pb, Ag, Cu, Ni, Fe, and Al was investigated by recycling 10% of E-waste with chalcopyrite. This highlighted some shortcoming of the actual databases, especially for the description of Ag in the matte phase, which has not yet been integrated in FactSage. As an approximation, an ideal solution between $Ag_2S(l)$ and the matte was considered to improve the realism of the simulations in this section.
- **Ti primary metal production from rutile**
  This section revealed the importance of using the full Gibbs energy minimization of a system instead of exploring specific chemical reactions to design pyrometallurgical processes. More specifically, the use of carbothermia to produce titanium is not a viable option because of the formation of TiC during the process for any operating conditions. The entire Kroll process was explored here using FactFlow. It involves the presence of a carbochlorination roasting to promote the production of $TiCl_4$. This product is further processed in a reduction unit with Mg to generate titanium sponges. A recovery rate of 96.6% (on a molar basis) when rutile is utilized as the raw material was evaluated from our simulations. Due to thermodynamic model limitations for the magnesiothermic unit, titanium partitioning was investigated with and without the presence of an ideal $MgCl_2$-$TiCl_2$ liquid solution. It was confirmed that this has no influence on the purity of the final product, as an excess of magnesium is often added in industrial operations, leading to the production of highly pure titanium.
- **MIDREX process modeling through stream recycling and virtual bypasses**
  The last example on the direct reduction of iron using the MIDREX process was specifically selected to showcase all the current functionalities that are available in the new FactFlow process simulator interface, *i.e.*, *Input*, *Exit* and *Recycle* nodes, *Equilibrium reactors*, *Mixer* and *Splitter* units as well as virtual bypasses. Our simulation primarily focused on the DRI furnace and the reformer unit.
  The approximation of the methane reforming kinetics via a virtual stream bypass was presented. Our simulations indicate that a virtual bypass factor $\gamma = 0.036$ closely matches available reforming data. Two virtual equilibrium counterflow reactors were employed to model the reduction process of the hematite-rich pellets with syngas. One virtual reactor (top) was operated at 650 °C while the other one (bottom) was at 950 °C. The simulation results were compared with data reported in the literature, showing good agreement in terms of iron metallization and $CO_2$ emissions.

In conclusion, the process simulations reported in this work illustrate the importance of computational thermochemistry coupled to an easy-to-use process simulator interface for the comprehensive analysis of pyrometallurgical processes. The final contribution of this series of papers (*i.e.*, part III) will extend the features of this computational thermochemistry tool to incorporate the following sophisticated modeling and optimization approaches:

- Implementation of the Effective Equilibrium Reaction Zone (EERZ) [79] to better integrate the kinetic description of pyrometallurgical unit operations.
- Coupling of the process flowsheet simulator to life cycle analysis inventories such as the Ecoinvent database [80] to quantify the total impact of pyrometallurgical processes.
- Construction of machine-learning models (surrogates) to speed up the exploration of operating conditions of complex process flowsheets.
- Integration of black-box optimization tools such as NOMAD [81] to identify optimal operating conditions for some multi-objective functions linked to operating costs, environmental impacts and product quality.

## CRediT authorship contribution statement

**Kyota Poëti:** Writing – original draft, Validation, Software, Methodology, Investigation, Formal analysis, Conceptualization. **Juan-Ricardo Castillo-Sánchez:** Writing – original draft, Validation, Methodology, Investigation, Formal analysis, Conceptualization. **Ugo Mahue:** Writing – original draft, Methodology, Investigation, Formal analysis, Conceptualization. **Vincent Rioux-Frenette:** Methodology, Investigation. **Zineb Squalli-Houssaini:** Investigation. **Kentaro Oishi:** Validation, Methodology, Conceptualization. **Jean-Philippe Harvey:** Writing – original draft, Validation, Supervision, Resources, Project administration, Methodology, Investigation, Funding acquisition, Formal analysis, Conceptualization.

## Declaration of competing interest

The authors declare the following financial interests/personal relationships which may be considered as potential competing interests: Jean-Philippe Harvey reports financial support was provided by Natural Sciences and Engineering Research Council of Canada. If there are other authors, they declare that they have no known competing financial interests or personal relationships that could have appeared to influence the work reported in this paper.

## Acknowledgments

We acknowledge the support of the Natural Sciences and Engineering Research Council of Canada (NSERC) *via* the Discovery Grant of Prof. Harvey (RGPIN-2017-06168). We extend our gratitude to Dr. Klaus Hack at GTT-Technologies for his thorough review of the manuscript and for providing insightful feedback.

## Appendix A. Supplementary data

Supplementary material related to this article can be found online at https://doi.org/10.1016/j.calphad.2024.102772.

## Data availability

The FactSage files (.equi) to generate the thermochemical data files (.cst) and the FactFlow files (.flow) to reproduce the simulations are provided in the Electronic Supplementary Material.

## References

[1] A. Ludwig, M. Wu, A. Kharicha, Simulation in metallurgical processing: Recent developments and future perspectives, JOM 68 (2016) 2191–2197.
[2] H.Y. Sohn, Principles and applications of mathematical and physical modelling of metallurgical processes, Miner. Process. Extr. Metall. 129 (2) (2020) 117–144.
[3] M.W. Kennedy, Metallurgical plant optimization through the use of flowsheet simulation modelling, in: Celebrating the Megascale: Proceedings of the Extraction and Processing Division Symposium on Pyrometallurgy in Honor of David GC Robertson, Springer, 2016, pp. 367–375.
[4] S. Spencer, H. Scriba, Best practices in process simulation for design of complex metallurgical plants, Metall. Plant Des. Oper. Strateg. (MetPlant 2008) (2008) 18–19.
[5] Home - METSIM – metsim.com, https://metsim.com/, [Accessed 09-01-2024].
[6] J. Bartlett, A. Holtzapple, C. Rempel, A brief overview of the process modelling/simulation and design capabilities of METSIM, in: Canadian Institute of Mining, Metallurgy and Petroleum: COM 2014-Conference of Metallurgists Proceedings, 2014.
[7] AVEVA - Global Leader in Industrial Software — aveva.com, https://www.aveva.com/en/, [Accessed 09-01-2024].
[8] Aspen HYSYS, | Process Simulation Software | AspenTech — aspentech.com, https://www.aspentech.com/en/products/engineering/aspen-hysys, [Accessed 09-01-2024].
[9] Plant Simulation Software | SysCAD — syscad.net, https://www.syscad.net/, [Accessed 09-01-2024].
[10] HSC-Sim | HSC Chemistry, https://www.metso.com/portfolio/hsc-chemistry/process-simulation-module/, [Accessed 10-03-2024].
[11] ChemApp Overview (SysCAD), https://help.syscad.net/ChemApp_Overview, [Accessed 22-10-2024].
[12] J.-P. Harvey, G. Eriksson, D. Orban, P. Chartrand, Global minimization of the gibbs energy of multicomponent systems involving the presence of order/disorder phase transitions, Am. J. Sci. 313 (3) (2013) 199–241.
[13] J.-R. Castillo-Sánchez, K. Oishi, L. St-Germain, D. Ait-Amer, J.-P. Harvey, The power of computational thermochemistry in high-temperature process design and optimization: Part 1—Unit operations, CALPHAD 82 (2023) 102593.
[14] J.-P. Harvey, A.E. Gheribi, Process simulation and control optimization of a blast furnace using classical thermodynamics combined to a direct search algorithm, Metall. Mater. Trans. B 45 (2014) 307–327.
[15] M.-A. Van Ende, Development of an electric arc furnace simulation model using the effective equilibrium reaction zone (EERZ) approach, JOM 74 (4) (2022) 1610–1623.
[16] J.-P. Harvey, F. Lebreux-Desilets, J. Marchand, K. Oishi, A.-F. Bouarab, C. Robelin, A.E. Gheribi, A.D. Pelton, On the application of the FactSage thermochemical software and databases in materials science and pyrometallurgy, Processes (ISSN: 2227-9717) 8 (9) (2020) http://dx.doi.org/10.3390/pr8091156, URL https://www.mdpi.com/2227-9717/8/9/1156.
[17] G. Khartcyzov, C. Kleeberg, M. Shevchenko, D. Shishin, E. Jak, Analysis of slag chemistry in WEEE smelting using experimental and modelling study of the "CuO0.5"-ZnO-FeO-FeO1.5-CaO-SiO2-AlO1.5 system in equilibrium with Cu metal, Ceram. Int. (ISSN: 0272-8842) 50 (15) (2024) 26513–26527, http://dx.doi.org/10.1016/j.ceramint.2024.04.380, URL https://www.sciencedirect.com/science/article/pii/S0272884224017802.
[18] D. Shishin, A.F. Mehrjardi, M. Shevchenko, T. Hidayat, E. Jak, Experimental study, thermodynamic calculations and industrial implications of slag/matte/metal equilibria in the Cu–Pb–Fe–O–S–Si system, J. Mater. Res. Technol. (ISSN: 2238-7854) 19 (2022) 899–912, http://dx.doi.org/10.1016/j.jmrt.2022.05.058, URL https://www.sciencedirect.com/science/article/pii/S2238785422007190.
[19] R. Jones, Computer Simulation of Pyrometallurgical Processes, Mintek, 1987.
[20] C. Bale, E. Bélisle, P. Chartrand, S. Decterov, G. Eriksson, A. Gheribi, K. Hack, I.-H. Jung, Y.-B. Kang, J. Melançon, A. Pelton, S. Petersen, C. Robelin, J. Sangster, P. Spencer, M.-A. Van Ende, Factsage thermochemical software and databases, 2010–2016, CALPHAD (ISSN: 0364-5916) 54 (2016) 35–53, http://dx.doi.org/10.1016/j.calphad.2016.05.002, URL http://www.sciencedirect.com/science/article/pii/S0364591616300694.
[21] I.-H. Jung, M.-A. Van Ende, Computational thermodynamic calculations: FactSage from CALPHAD thermodynamic database to virtual process simulation, Metall. Mater. Trans. B 51 (2020) 1851–1874.
[22] A.K. Shukla, Thermodynamics-based modeling of iron-and steelmaking processes using flow sheet-based approach employing METSIM, Trans. Indian Inst. Met. 72 (2019) 767–775.
[23] K. Hack, M.-A. Van Ende, Chapter 5.4 - process modeling, in: S. Seetharaman (Ed.), Treatise on Process Metallurgy, Elsevier, Boston, ISBN: 978-0-08-096984-8, 2014, pp. 799–852, http://dx.doi.org/10.1016/B978-0-08-096984-8.00033-1, URL https://www.sciencedirect.com/science/article/pii/B9780080969848000331.
[24] A. Kumar, V. Thapliyal, D.G. Robertson, J.D. Smith, Kinetics of corrosion of BN–ZrO2–SiC ceramics in contact with si-killed steel, J. Am. Ceram. Soc. 98 (5) (2015) 1596–1603.
[25] J.Z. Khoo, N. Haque, S. Bhattacharya, Process simulation and exergy analysis of two nickel laterite processing technologies, Int. J. Miner. Process. 161 (2017) 83–93.
[26] D. You, S.K. Michelic, C. Bernhard, Modeling of ladle refining process considering mixing and chemical reaction, Steel Res. Int. 91 (11) (2020) 2000045.
[27] C. Yilmaz, J. Wendelstorf, T. Turek, Modeling and simulation of hydrogen injection into a blast furnace to reduce carbon dioxide emissions, J. Clean. Prod. 154 (2017) 488–501.
[28] Y. Yang, Z. Wang, L. Guo, X. Wen, Z. Guo, Proposal and analysis of a polygeneration process for coal gasification and ironmaking, Sustain. Energy Technol. Assess. 51 (2022) 101901.
[29] V. Singh, L.C. Buelens, H. Poelman, M. Saeys, G.B. Marin, V.V. Galvita, Carbon monoxide production using a steel mill gas in a combined chemical looping process, J. Energy Chem. 68 (2022) 811–825.
[30] M. Bailera, P. Lisbona, B. Peña, L.M. Romeo, A review on CO2 mitigation in the iron and steel industry through power to X processes, J. CO2 Util. 46 (2021) 101456.
[31] N. Tripathi, E. Peek, M. Stroud, Advanced process modeling at the BCL smelter: Improving economic and environmental performance, Jom 63 (2011) 63–67.
[32] D. Pashchenko, Thermodynamic equilibrium analysis of steam methane reforming based on a conjugate solution of material balance and law action mass equations with the detailed energy balance, Int. J. Energy Res. 44 (1) (2020) 438–447.
[33] S. Petersen, K. Hack, The thermochemistry library ChemApp and its applications, Int. J. Mater. Res. 98 (10) (2007) 935–945.
[34] G. Eriksson, E. Königsberger, FactSage and ChemApp: Two tools for the prediction of multiphase chemical equilibria in solutions, Pure Appl. Chem. 80 (6) (2008) 1293–1302.
[35] Qt Creator, Embedded Software Development Tools & Cross Platform IDE, https://www.qt.io/product/development-tools, [Accessed 25-01-2024].
[36] B. Stroustrup, The C++ Programming Language, Pearson Education, 2013.
[37] S. Yadav, C. Srishilan, A.K. Shukla, Thermodynamic model of MIDREX ironmaking process using FactSageTM and macro facility, Metall. Mater. Trans. B 54 (6) (2023) 3508–3525.
[38] B. Machulec, Equilibrium model of the ferrosilicon melting process in the submerged arc-resistance furnace, in: Proc. 10 Intern. Conf. Advanced Metods in the Theory of Electrical Eng. Pilsen: University of West Bohemia, 2011.
[39] B. Machulec, S. Gil, W. Bialik, Equilibrium model of the ferrosiliucon process in the submerged arc furnace, in: 27th International Conference on Metallurgy and Materials, METAL, 2018, pp. 122–127.
[40] A.D. Pelton, C.W. Bale, J. Melançon, G. Eriksson, K. Hack, M. to Baben, Applying constraints to chemical equilibrium calculations through the use of virtual elements, CALPHAD (ISSN: 0364-5916) 81 (2023) 102544, http://dx.doi.org/10.1016/j.calphad.2023.102544, URL https://www.sciencedirect.com/science/article/pii/S0364591623000160.
[41] Y. Wang, A. Karasev, J.H. Park, P.G. Jönsson, Non-metallic inclusions in different ferroalloys and their effect on the steel quality: A review, Metall. Mater. Trans. B 52 (2021) 2892–2925.
[42] A. Schei, J.K. Tuset, H. Tveit, et al., Production of High Silicon Alloys, Tapir Trondheim, 1998.
[43] R.E. Brown, Magnesium and its alloys, in: Mechanical Engineers' Handbook, Volume 1: Materials and Engineering Mechanics, John Wiley & Sons, 2015, p. 289.

[44] N. Batra, Modelling of ferrosilicon smelting in submerged arc furnaces, Ironmak. Steelmak. 30 (5) (2003) 399–404.
[45] B. Machulec, W. Bialik, Model of the ferrosilicon melting process in the submerged arc furnace, in: International Conference on Innovative Technologies, in-TECH, 2012, pp. 26–28.
[46] D. Senapati, E.U. Maheswar, C. Ray, Ferro silicon operation at IMFA–a critical analysis, in: International Ferro-Alloys Congress Infacon XI, New Delhi, India, 2007, pp. 371–380.
[47] W.G. Davenport, M.J. King, M.E. Schlesinger, A.K. Biswas, Extractive metallurgy of copper, Elsevier, 2002.
[48] R. Moskalyk, A. Alfantazi, Review of copper pyrometallurgical practice: today and tomorrow, Miner. Eng. 16 (10) (2003) 893–919.
[49] A. Klassert, L. Tikana, Copper and copper–nickel alloys–an overview, Corros. Behav. Prot. Copp. Alum. Alloy. Seawater (2007) 47–61.
[50] Our operations, GLENCORE Canada, [Accessed 10-01-2024]. URL https://www.glencore.ca/en/horne/ce-que-nous-faisons/nos-operations.
[51] J. Wood, S. Creedy, R. Matusewicz, M. Reuter, Secondary copper processing using outotec ausmelt TSL technology, Proc. MetPlant (2011) 460–467.
[52] A. Khaliq, M.A. Rhamdhani, G. Brooks, S. Masood, Metal extraction processes for electronic waste and existing industrial routes: a review and Australian perspective, Resour. 3 (1) (2014) 152–179.
[53] B. Desai, V. Tathavadkar, S. Basu, Selenium partitioning between slag and matte during smelting, Russ. J. Non-Ferrous Met. 57 (4) (2016) 325–330.
[54] M.E. Schlesinger, K.C. Sole, W.G. Davenport, G.R.A. Flores, Extractive metallurgy of copper, Elsevier, 2021.
[55] Y. Sun, M. Chen, E. Balladares, C. Pizarro, L. Contreras, B. Zhao, Effect of MgO on the liquid/spinel/matte/gas equilibria in the Si–Fe–Mg–O–Cu–S system at controlled P(SO2) 0.3 and 0.6 atm, CALPHAD (ISSN: 0364-5916) 70 (2020) 101803, http://dx.doi.org/10.1016/j.calphad.2020.101803, URL https://www.sciencedirect.com/science/article/pii/S0364591620300687.
[56] J. Van Yken, N.J. Boxall, K.Y. Cheng, A.N. Nikoloski, N.R. Moheimani, A.H. Kaksonen, E-waste recycling and resource recovery: A review on technologies, barriers and enablers with a focus on oceania, Metals 11 (8) (2021) 1313.
[57] M. Shuva, M. Rhamdhani, G. Brooks, S. Masood, M. Reuter, Thermodynamics data of valuable elements relevant to e-waste processing through primary and secondary copper production: a review, Journal of cleaner production 131 (2016) 795–809.
[58] C.B. Tabelin, I. Park, T. Phengsaart, S. Jeon, M. Villacorte-Tabelin, D. Alonzo, K. Yoo, M. Ito, N. Hiroyoshi, Copper and critical metals production from porphyry ores and E-wastes: A review of resource availability, processing/recycling challenges, socio-environmental aspects, and sustainability issues, Resour. Conserv. Recy. 170 (2021) 105610.
[59] F. Faraji, R. Golmohammadzadeh, C.A. Pickles, Potential and current practices of recycling waste printed circuit boards: a review of the recent progress in pyrometallurgy, J. Environ. Manag. 316 (2022) 115242.
[60] G. Lütjering, J.C. Williams, Titanium, Springer Science & Business Media, 2007.
[61] C. Leyens, M. Peters, Titanium and titanium alloys: fundamentals and applications, Wiley Online Library, 2006.
[62] R. Boyer, Attributes, characteristics, and applications of titanium and its alloys, Jom 62 (5) (2010) 21–24.
[63] T. Smijs, S. Pavel, A case study: Nano-sized titanium dioxide in sunscreens, Nanoeng. (2015) 375–423.
[64] W. Zhang, Z. Zhu, C.Y. Cheng, A literature review of titanium metallurgical processes, Hydrometall. 108 (3–4) (2011) 177–188.
[65] J. Gambogi, Titanium mineral concentrates, US Geol. Surv. Miner. Commod. Summ. 2020 (2020) 176–177.
[66] A. Baba, S. Swaroopa, M. Ghosh, F. Adekola, Mineralogical characterization and leaching behavior of Nigerian ilmenite ore, Trans. Nonferr. Met. Soc. China 23 (9) (2013) 2743–2750.
[67] D.L. Price, B.R. Cooper, J.M. Wills, Full-potential linear-muffin-tin-orbital study of brittle fracture in titanium carbide, Phys. Rev. B 46 (1992) 11368–11375, http://dx.doi.org/10.1103/PhysRevB.46.11368.
[68] D. Fray, Novel methods for the production of titanium, Int. Mater. Rev. 53 (6) (2008) 317–325.
[69] T.H. Okabe, O. Takeda, Fundamentals of thermochemical reduction of TiCl4, in: Extractive Metallurgy of Titanium, Elsevier, 2020, pp. 65–95.
[70] O. Takeda, T. Uda, T.H. Okabe, Rare earth, titanium group metals, and reactive metals production, in: Treatise on Process Metallurgy, Elsevier Ltd, 2014, pp. 995–1069.
[71] A. Fuwa, S. Takaya, JOM 57 (10) (2005) 56–60, http://dx.doi.org/10.1007/s11837-005-0153-7.
[72] Y. Song, Z. Dou, T.-a. Zhang, Y. Liu, Research progress on the extractive metallurgy of titanium and its alloys, Miner. Process. Extr. Metall. Review (2020) 1–17.
[73] M. Atsushi, H. Uemura, T. Sakaguchi, MIDREX processes, Kobelco Technol. Rev. 29 (2010) 50–57.
[74] N. Pardo, J.A. Moya, Prospective scenarios on energy efficiency and CO2 emissions in the European iron & steel industry, Energy 54 (2013) 113–128.
[75] M. Flores-Granobles, M. Saeys, Minimizing CO2 emissions with renewable energy: a comparative study of emerging technologies in the steel industry, Energy Environ. Sci. 13 (7) (2020) 1923–1932.
[76] M. Shahabuddin, G. Brooks, M.A. Rhamdhani, Decarbonisation and hydrogen integration of steel industries: Recent development, challenges and technoeconomic analysis, J. Clean. Prod. (ISSN: 0959-6526) 395 (2023) 136391, http://dx.doi.org/10.1016/j.jclepro.2023.136391, URL https://www.sciencedirect.com/science/article/pii/S0959652623005498.
[77] E. Sadatshojaei, F. Esmaeilzadeh, J. Fathikaljahi, S.E. Hosseynian Barzi, D.A. Wood, Regeneration of the midrex reformer catalysts using supercritical carbon dioxide, Chem. Eng. J. (ISSN: 1385-8947) 343 (2018) 748–758, http://dx.doi.org/10.1016/j.cej.2018.02.038, URL https://www.sciencedirect.com/science/article/pii/S138589471830233X.
[78] N.I. Bond, R.T. Symonds, R.D. Hughes, Pressurized Chemical Looping for Direct Reduced Iron Production: Carbon Neutral Process Configuration and Performance, Energies 15 (14) (2022) 5219, http://dx.doi.org/10.3390/en15145219.
[79] M.-A. Van Ende, Y.-M. Kim, M.-K. Cho, J. Choi, I.-H. Jung, A kinetic model for the ruhrstahl heraeus (RH) degassing process, Metall. Mater. Trans. B 42 (2011) 477–489.
[80] G. Wernet, C. Bauer, B. Steubing, J. Reinhard, E. Moreno-Ruiz, B. Weidema, The ecoinvent database version 3 (part i): overview and methodology, Int. J. Life Cycle Assess. 21 (2016) 1218–1230.
[81] C. Audet, S. Le Digabel, V. Rochon Montplaisir, C. Tribes, Algorithm 1027: NOMAD version 4: Nonlinear optimization with the MADS algorithm, ACM Trans. Math. Softw. 48 (3) (2022) 35:1–35:22, http://dx.doi.org/10.1145/3544489.